UNIVERSITY OF OKLAHOMA

GRADUATE COLLEGE

APPLICATION OF SEISMIC ATTRIBUTES AND UNSUPERVISED MACHINE LEARNING METHODS FOR IDENTIFICATION OF HIDDEN FAULTS IN BASEMENT AND CARBONATE ROCKS

A THESIS

SUBMITTED TO THE GRADUATE FACULTY

in partial fulfillment of the requirements for the

Degree of

MASTER OF SCIENCE

By

DIANA KATERINE SALAZAR FLOREZ

Norman, Oklahoma

2023

APPLICATION OF SEISMIC ATTRIBUTES AND UNSUPERVISED MACHINE LEARNING METHODS FOR IDENTIFICATION OF HIDDEN FAULTS IN BASEMENT AND CARBONATE ROCKS

A THESIS APPROVED FOR THE

SCHOOL OF GEOSCIENCES

BY THE COMMITTEE CONSISTING OF

Dr. Heather Bedle, Chair

Dr. Brett M. Carpenter

Dr. Jacob Walter

To mom and dad

ACKNOWLEDGEMENTS

I would like to start by expressing my deepest gratitude to my advisor Dr. Heather Bedle. She trusted me when I was an undergrad student and since then she continued to believe in me, support me, understand me when the moments were tough, and provide me with many opportunities as a graduate student, both professionally and personally. I will always be grateful to her because my biggest and most important achievements were thanks to the outcomes of our work together.

To Dr. Carpenter and Dr. Walter, thank you so much for serving on my committee. I could not be more grateful to Dr. C for the uncountable meetings and his willingness to help; his guidance and advice were crucial during the final and most critical stage of this work.

To the School of Geosciences at the University of Oklahoma, the Mewbourne College of Earth and Energy, the Colombian Student Association, the Graduate College, and the Society of Exploration Geophysicist, for providing me with scholarships and awards that were of great help for my academic and professional development.

To my closest friends Pamela Blanco, Miguel Romero, Ronnie and Karen Martinez, and Alayna Wong. Thanks for being my family here, for cheering me up, helping me take breaks, and especially for reminding me of the life outside my studies. Thanks to Gloria and Mitch Burrus for all the evenings, OU games, and Thanksgiving spent together.

To my friends and colleagues from the School of Geosciences and AASPI, Raymond Ng, Mario Ballinas, Ganiyat Shodunke, Laura Ortiz, David Lubo, Emily Jackson, Grace Barber, Marcus Maas, Alex Vera, Karelia La Marca, Bobby Buist, and many others. Thanks for your advice, support, and many other moments of happiness shared.

Lastly, and most importantly, my very loved ones. My parents, who no matter the adversities did everything they could to take me where I am, a very proud first-generation child who is now getting her master's. My sister, who has been chasing her dreams for years and has fought many battles is more than an inspiration to me, but a role model. And my husband, *mon amour,* who was able to understand me more than anyone and was there every single time.

TABLE OF CONTENT

LIST OF FIGURES

LIST OF TABLES

ABSTRACT

Seismic fault interpretation is a critical task for any type of energy industry and correct fault mapping can be crucial for the success of a project. Common geometric seismic attributes such as coherence and curvature are routinely employed to enhance fault visualization in seismic data, but they can show limitations for sub-seismic faulting. Two projects are presented here showing how recently introduced geometric seismic attributes, such as total aberrancy, and unsupervised machine learning methods, such as self-organizing maps (SOM) and generative topographic mapping (GTM), can be applied for enhancing fault visualization.

The first project focuses on an area with potential for CO2 storage in the carbonates of the Duperow Formation, northern Montana. In this study, we compared broadband and multispectral coherence, curvature, and aberrancy, and we compared SOM and GTM techniques when including and excluding aberrancy attributes. Our results showed that integrating aberrancy attributes during the multiattribute analysis and the machine learning steps considerably enhance the visualization of lineaments with strikes similar to those of fracture sets seen only with well log data and missed by the conventional geometric seismic attributes and the ML scenarios excluding aberrancy attributes.

The second project is related to wastewater injection and induced seismicity in basement-rooted faults in northcentral Oklahoma. Here, different geometric seismic attributes were analyzed and integrated using unsupervised machine learning to identify potential basement-rooted faults and strike-slip-related structures. The machine learning results not only confirmed the existence of NE-SW faults that extend from the basement upward into the sedimentary section and that correlated with earthquake data but also the potential existence of other NE-SW structurally controlled features of anticlinorium shape.

CHAPTER 1. APPLICATION OF A NOVEL GEOMETRIC SEISMIC ATTRIBUTE FOR ENHANCING FAULT VISUALIZATION IN AREAS OF POTENTIAL CARBON CAPTURE AND STORAGE

ABSTRACT

Seismic fault interpretation is a critical task for any type of energy industry and correct fault mapping can be crucial for the success of a project. Common geometric seismic attributes such as coherence and curvature are routinely employed to enhance fault visualization in seismic data, but they can present limitations for sub-seismic faulting. In this study, we highlight the usefulness of including the more novel aberrancy attributes for fault identification in multiattribute analysis and unsupervised machine learning techniques. We compare broadband coherence, curvature, multispectral coherence, and aberrancy when trying to map faults in a potential CO_2 storage location, and we compare self-organizing maps (SOM) and generative topographic mapping (GTM) techniques when including and excluding aberrancy attributes. Our results show that integrating aberrancy attributes during the multiattribute analysis and the machine learning steps considerably enhance the visualization of lineaments with strikes similar to those of fracture sets seen only with well log data. These lineaments were missed by the conventional geometric seismic attributes and the ML scenarios excluding aberrancy attributes. We demonstrate the potential of these novel geometric seismic attributes to map sub-seismic faults as well as provide an example that can encourage interpreters to include them in their interpretation workflows.

INTRODUCTION

Fault mapping is fundamental to identify trap mechanisms, potential leak points, migration pathways, and to understand the structural setting of an area of interest, regardless of whether the target is oil and gas production, CO_2 geological storage, or injection of fluids for enhanced oil/gas recovery and geothermal energy. Failing to correctly identify faults and fractures in the rock may have consequences from losing control of injected fluid, to inducing seismicity (Kay et al. 1993; Ellsworth, 2013). Seismic attributes such as coherence and curvature are systematically applied for structural seismic interpretation since they have a very well-documented record of successful case studies (Gupta et al. 2013; Schneider et al. 2016; Libak et al. 2017; and Karam et al. 2021). However, these attributes fail to properly image faults for which vertical offset is below seismic resolution. Multispectral coherence and aberrancy have been more recently introduced to help in cases where fault offset is lost in the frequency content or seen only as small bends with no clear discontinuity, respectively (Gao and Di, 2015; Li et al., 2018; and Lyu et al., 2020). Due to these capabilities, these attributes are showing promising results in helping interpreters detect potential faults in scenarios of sub-seismic offsets.

For this study, we use the P-wave component of the multicomponent Kevin Dome dataset located in the region of the Sweetgrass Arch, Montana, U.S (Figure 1-1A). Kevin Dome is a large structural closure that naturally traps CO_2 in the Devonian naturally fractured and interbedded limestone/dolostone Duperow Formation (Zaluski, 2018). As part of a partnership between the Big Sky Carbon Sequestration Partnership (BSCSP) and the U.S. Department of Energy (DOE), this region was identified as an ideal site to study additional underground storage of anthropogenic CO_2. The initial phases of the project aimed to extract the naturally accumulated CO_2 (Danielson 33-17, CO_2 production well) and re-inject it (Wallewein 22-1, CO_2 injector well) on the brine-filled side of the Duperow Formation (Figure 1-1B), with the objective of evaluating the viability, injectivity capacity, and storability on the target formation and other analogous formations (Onishi et al., 2019). Although EPA regulations did not allow for the storage of anthropogenic CO_2 in Duperow, BSCSP altered the focus of the project to collecting data that aid in characterization of the reservoir (from well logs to cores) along with seismic data.

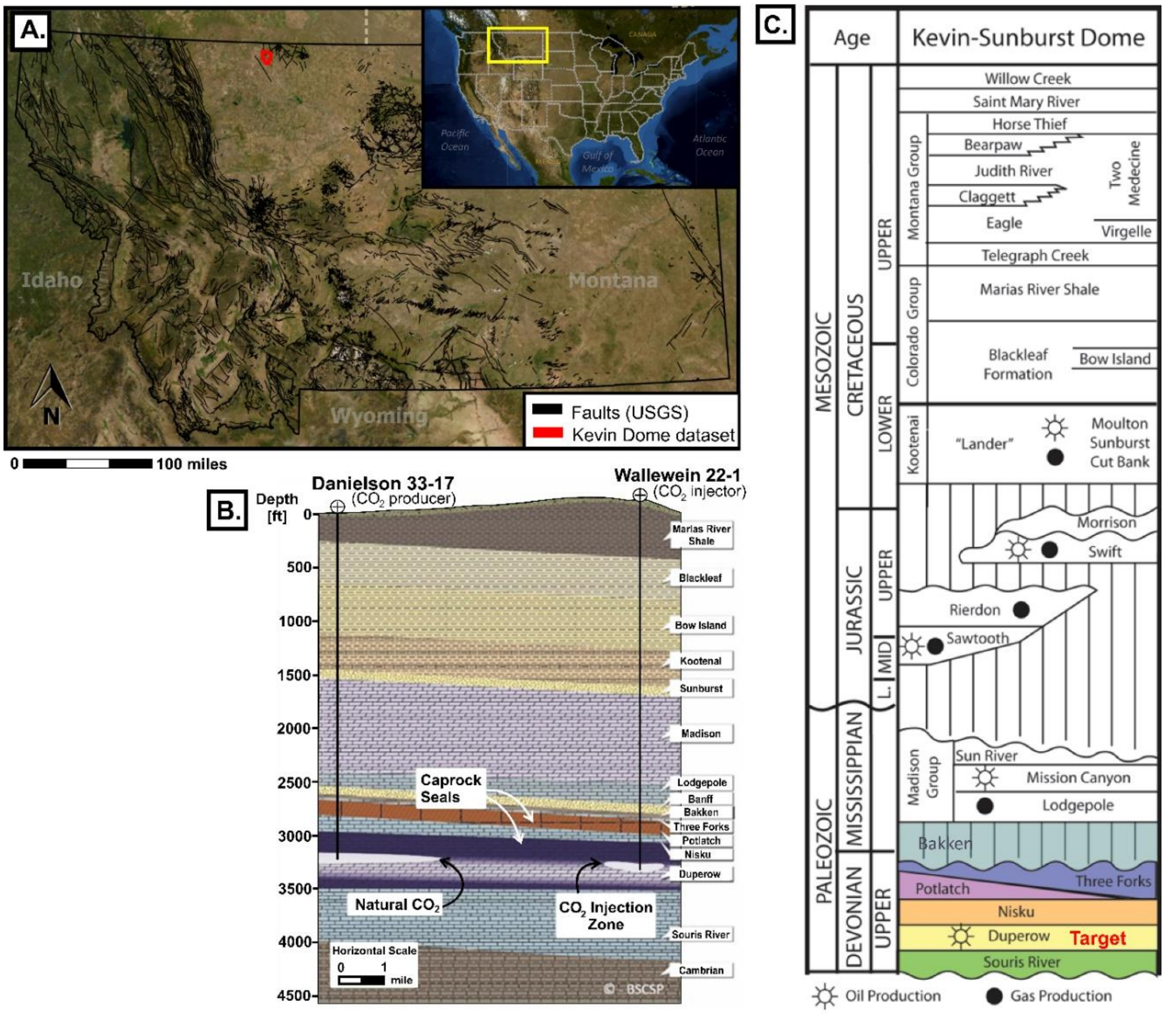

Figure 1-1. A) Location of Kevin Dome seismic dataset within the state of Montana, B) generalized representation of the Kevin Dome subsurface and the project initially envisioned by the BSCSP (modified from Onishi et al. 2019), C) stratigraphic column in the Kevin Dome area (modified from Clochard et al. 2018).

In this seismic dataset, three main N-S fault trends are seen to clearly cut the reflectors below the target zone (Figure 1-2, F1, F2, F3). However, previous reports that integrate different types of available data into a static model indicate these faults are sealing faults that do cut the injection interval (Zaluski, 2018). Moreover, FMI logs highlighted the existence of fractures with NE-SW and NW-SE strikes, which are not obvious in the seismic amplitude volume. For these two reasons, we found this dataset appropriate to test the capabilities of aberrancy attributes and unsupervised machine learning (ML) methods to enhance fault visualization in carbonate rocks suitable for CO_2 storage. This study expands upon a previous work included in Bedle et al. (2022), which covered only the multiattribute analysis step. Here, we present both the multiattribute analysis and the different machine learning tests.

Dataset

The Kevin Dome dataset is a 3D multicomponent seismic survey of which we focused only on the primary P-wave pre-stack time migrated seismic volume. The seismic volume has a bin size of 55 x 55 ft, a record length of 2 seconds, and a sample interval of 2 milliseconds. Figure 1-2A shows the horizon probe created for the purpose of this study as well as the three faults (F1, F2, and F3) cutting the seismic reflectors below the target Duperow Formation.

For the purpose of this study, previous fracture analysis performed with FMI data from the wells Danielson 33-17 and Wallewein 22-1 will also be included. The location of these wells is shown in Figure 1-2B, and the details of the FMI analysis can be found in Zaluski (2018).

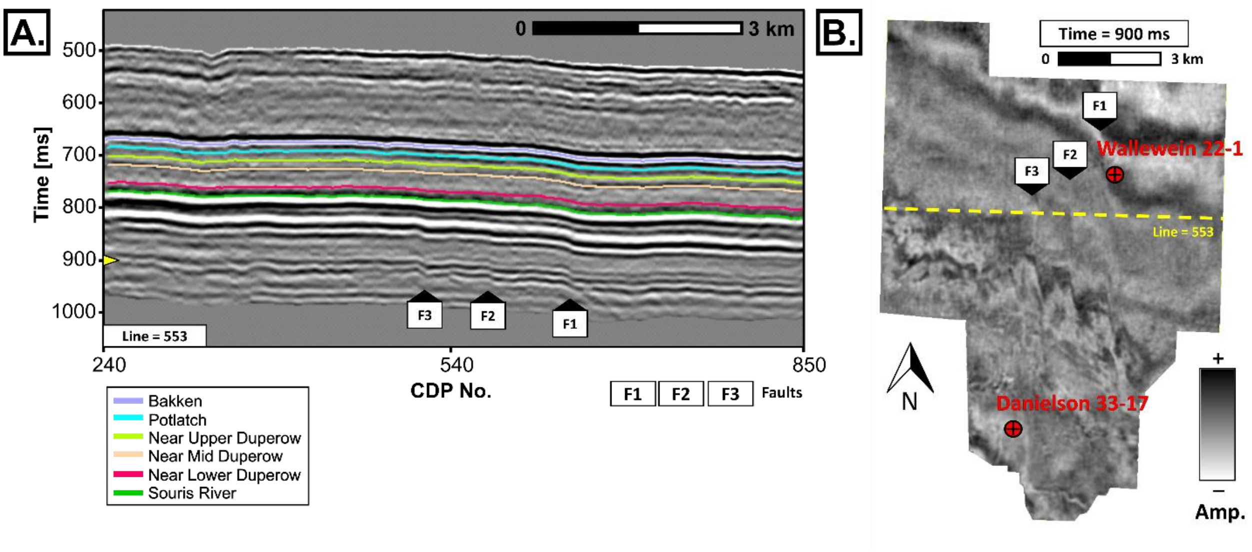

Figure 1-2. Horizon probe covering the area of interest, the Duperow formation, and stratal mapping of surfaces compared to mapped horizons of Zaluski (2018). Note the faults (F1, F2, F3) below the target zone. Modified from Bedle et al. (2022).

METHODOLOGY

In this study, we highlight the usefulness of including aberrancy attributes for fault identification when doing multiattribute analysis and applying unsupervised machine learning (ML) techniques such as self-organizing maps (SOM) and generative topographic mapping (GTM). During the multiattribute analysis stage, we compare broadband coherence, k1-most positive and k2-most negative curvature, multispectral coherence, and aberrancy azimuth and magnitude; and during the ML stage, we compare SOM and GTM techniques when including and excluding aberrancy attributes (Figure 1-3).

Before calculating any seismic attribute, and as part of a conditioning step, we first applied two filters to remove coherent (acquisition footprint removal filter; Falconer and Marfurt, 2008) and random noise (structure-oriented filter; Luo et al. 2002 and Fehmers and Höcker, 2003), one pass in each filter to avoid removing smaller scale features that could be related to geological content. After those two conditioning steps, we proceed to map the horizons of interest taking as reference surfaces mapped by Zaluski (2018). We focus on Bakken, Potlach, Upper Duperow, Mid Duperow, Lower Duperow, and Souris River; although we mapped two additional seismic reflectors above and below the target zones in order to create a seismic horizon probe that would serve as input for the next steps.

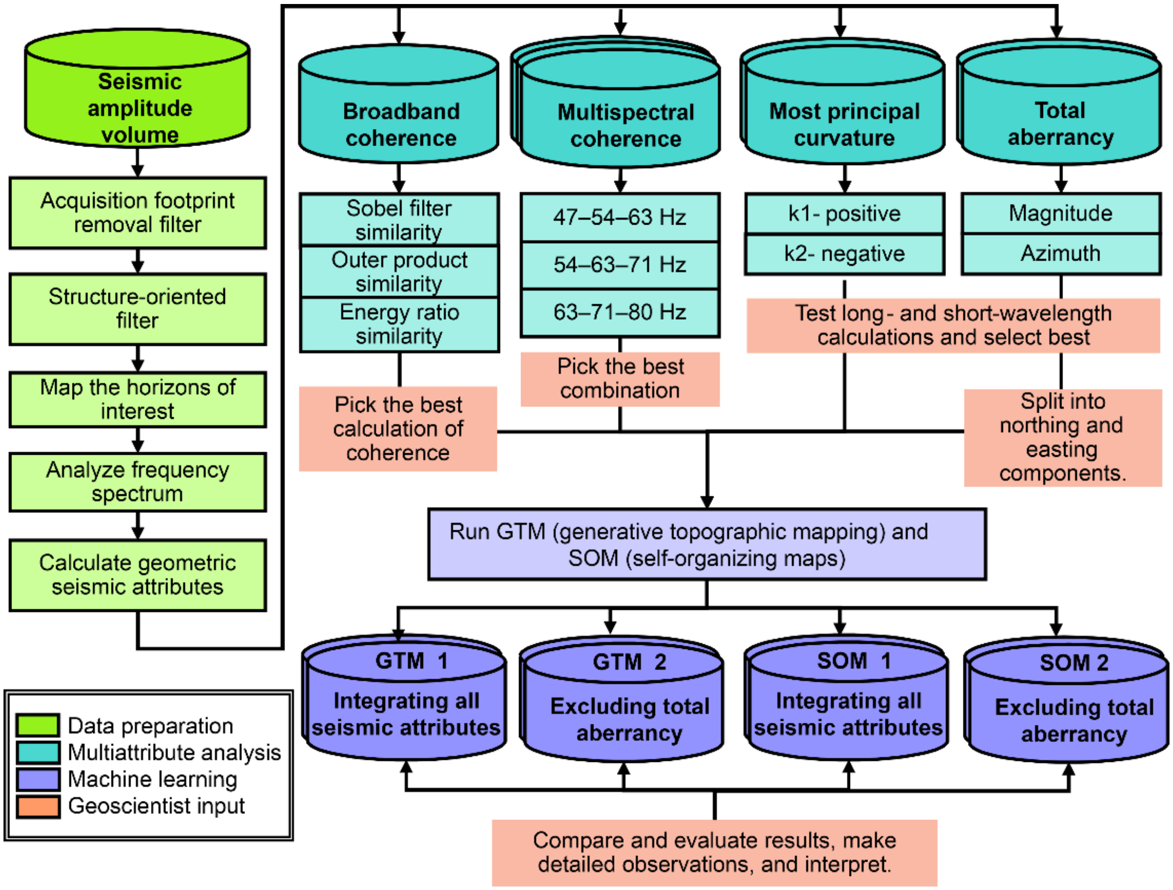

Figure 1-3. Workflow followed.

We then proceed to calculate the conventional geometric attributes of broadband coherence, multispectral coherence, and curvature, and the most novel aberrancy attributes. For the multispectral coherence, we started by first analyzing the frequency spectrum (constrained to the target interval and middle to higher frequencies, as we are interested in small scale features), selecting the spectral voices of interest, and creating different combinations using RGB (red-green-blue) blends to finally select the combination that better highlights geological content.

Finally, we ran two unsupervised methods: SOM and GTM. Four tests are made, two for each method, with the objective of comparing results when including all attributes calculated (SOM 1 and GTM 1) and when excluding aberrancy attributes (SOM 2 and GTM 2). Table 1-1 shows the scenarios created and the specific seismic attributes included in each case.

SOM 1 and GTM 1	SOM 2 and GTM 2
Sobel filter similarity broadband	Sobel filter similarity broadband
k1-most positive principal curvature	k1-most positive principal curvature
k2-most negative principal curvature	k2-most negative principal curvature
Total aberrancy magnitude *	Sobel filter similarity 54 Hz
Total aberrancy azimuth *	Sobel filter similarity 63 Hz
Sobel filter similarity 54 Hz	Sobel filter similarity 71 Hz
Sobel filter similarity 63 Hz	
Sobel filter similarity 71 Hz	

Table 1-1. Case scenarios created using SOM and GTM to test the capabilities of integrating conventional and novel geometric seismic attributes for fault visualization enhancement. SOM 1 and GTM 1 including all geometric attributes and SOM 2 and GTM 2 excluding aberrancy attributes. *Aberrancy attributes were included using the mathematical conversion explained in the seismic attributes section.

Seismic Attributes

Since we are interested in enhancing the visualization of structural features only, we will focus solely on geometric seismic attributes as they have proved to be best for seismic structural interpretation. The seismic attributes considered to aid in the interpretations are: 1) broadband coherence, 2) coherence at 54 Hz, 3) coherence at 63 Hz, 4) coherence at 71 Hz, 5) k1-most positive principal curvature, 6) k2-most negative principal curvature, 7) aberrancy azimuth, and 8) aberrancy magnitude. The mathematical relationship between the coherence, curvature, and aberrancy can be visualized in Figure 1-4, as well as the fault expression they highlight in the seismic data. Dip is the most important constraint when calculating coherence, curvature, and aberrancy (Chopra and Marfurt, 2020).

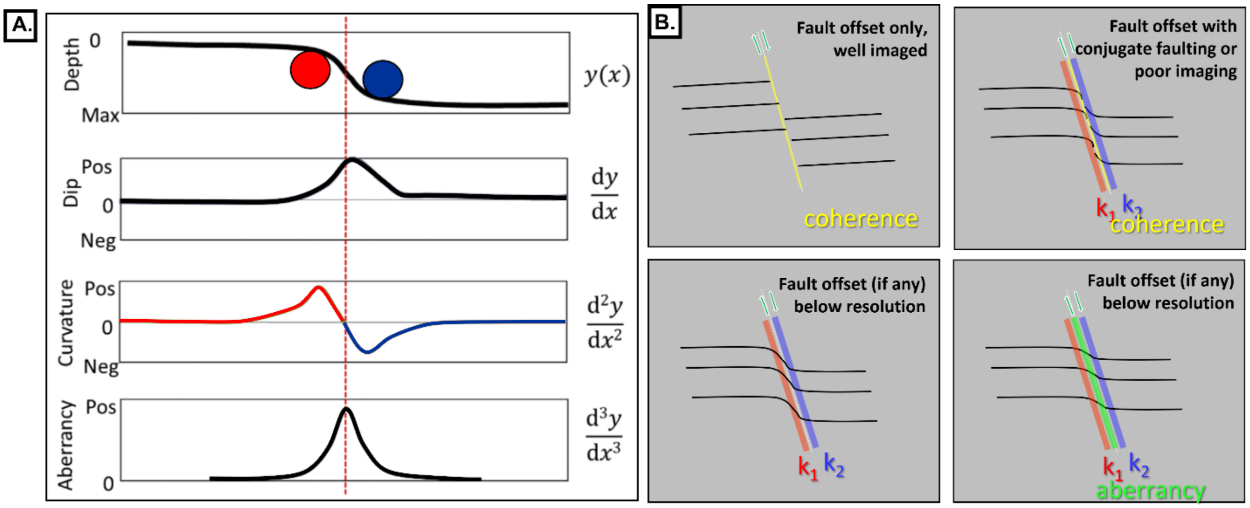

Figure 1-4. Relationship between the different geometric seismic attributes. A) mathematical concept of the geometric attributes, after Bhattacharya and Verma (2019), and B) geological relationship of attributes and faults, modified from Patel et al. (2021).

Broadband coherence is calculated over the full-bandwidth volume by measuring the similarity of neighboring traces (Bahorich and Farmer, 1995). It works very well when there is a clear discontinuity in the reflectors, and it has been proved to work not only with faults but also with stratigraphic edges such as the borders of a channel. Multispectral coherence uses the same approach as broadband coherence, but it is calculated from different spectral voice components. It shows features that may have been lost within the broadband seismic (Li et al., 2018).

Similar to coherence, curvature can also be applied for structural and stratigraphic features. When used for stratigraphic features, k1-most positive curvature helps to identify anticlinal and domal features, while and k2- most negative curvature help with synclinal and bowl-like features (Chopra and Marfurt, 2007). Curvature works for structural features when the seismic expression of the fault is characterized by folded reflectors on each side of the fault (Chopra and Marfurt, 2011). More specifically, upthrown-sides will have a positive anomaly captured by k1-most positive curvature while the downthrown-side will have a negative anomaly captured by k2- most negative curvature.

Aberrancy is a more novel technique that was introduced by Gao et al. (2013) as an extension and complement of the existing curvature attribute. It is able to map planes of potential sub-seismic faults, whose seismic expression in the seismic amplitude volume is a subtle flexure of the reflector rather than a discontinuity; this would be the case for faults with vertical offset below seismic resolution (Gao and Di, 2015; Qi and Marfurt, 2018; Bhattacharya and Verma, 2019).

For the ML workflow, the aberrancy azimuth and the aberrancy magnitude will be integrated differently. Since aberrancy azimuth is a cyclical attribute, values of -180° and 180° will be considered the same after the normalization step prior to the ML application. In that sense, we separate the vector in its northing [1] and easting [2] components by applying the following equations:

$$Total\ aberrancy\ magnitude \times sin(Total\ aberrancy\ azimuth) \qquad [1]$$

$$Total\ aberrancy\ magnitude \times cos\ \ (Total\ aberrancy\ azimuth) \qquad [2]$$

Machine Learning Methods

Most of the studies that focus on the application of unsupervised ML methods in seismic data do so for seismic facies classification (Zhao et al. 2015; Maas et al. 2023, Lubo et al. 2023). However, fault identification may not necessarily fall into a different type of geoscience problem. We have seen that different fault expressions in the seismic amplitude volume may be visualized using different seismic attributes. In that sense, integrating all seismic attributes using ML could be a helpful way to find all different seismic fault patterns using a single volume rather than having to interpret in several seismic volumes that may as well correspond to a co-render of two or three different seismic attributes.

A study of such was performed by Hussein et al. (2020), in which the authors probe the success of SOM for fault visualization enhancement using multispectral coherence, dip magnitude, aberrancy magnitude, curvedness, GLCM entropy, and GLCM homogeneity. Here, we will further test GTM method as well as other seismic attribute combinations, as mentioned in the previous section.

Self-Organizing Maps (SOM)

SOM is considered a projection technique for dimensionality reduction that helps in understanding high dimensional data through less complex outputs, such as for data visualization, clustering, and pattern recognition applications. A detailed mathematical explanation of SOM can be found in Kohonen (1982) while a user-friendly review and applications in geoscience is presented by Roy et al. (2011).

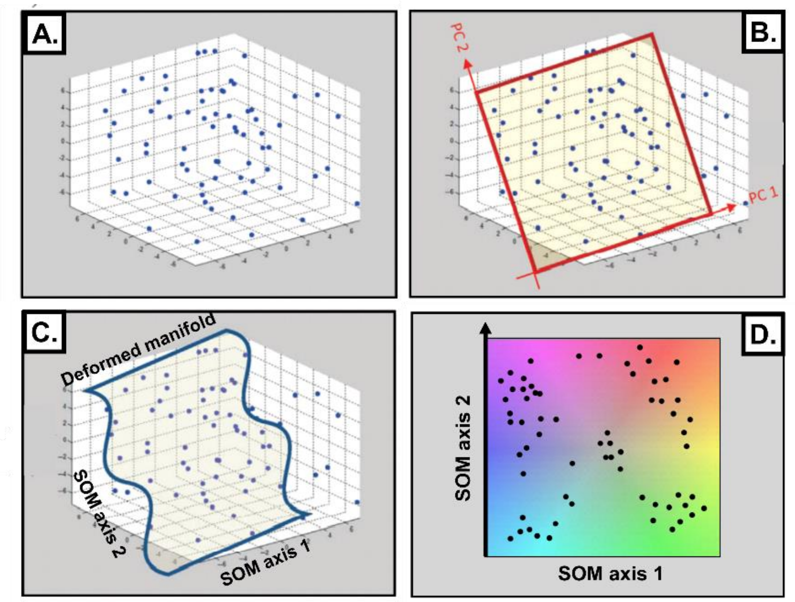

Figure 1-5. Simplified projection steps in SOM, A) data is plotted in a multidimensional space, B) eigenvectors are computed and the principal components (PC) are determined to further select the initial manifold and start populating it with prototype vectors, C) manifold deforms to fit the natural clusters, D) prototype vectors are mapped against a 2D color bar (modified from Zhao et al. 2015b).

SOM starts by plotting the N-dimensional input data into an N-dimensional space (Figure 1-5A). By using principal component analysis, the main directions of variability are computed, and the first components are defined by organizing the eigenvectors through their eigenvalues. The first two eigenvectors (principal components) are used to define the 2D latent space in which the input data will be projected (Figure 1-5B). During training, this latent space deforms, therefore called a manifold, to better represent the data (Figure 1-5C). After several iterations, the model finds convergence, and clustering is possible by assigning a 2D color bar (5D). In that sense, data with similar colors is associated to patterns of similar nature, while data with different colors is interpreted to be associated with different features (Roy et al. 2011).

Despite their widely recognized applications, and as stated by different authors, SOM has different limitations both during training and clustering (Roy et al. 2014, Zhao et al, 2015; and Chopra and Marfurt, 2018c). GTM was introduced by Bishop et al. (1998) to solve for most of the SOM drawbacks.

Generative Topographic Mapping (GTM)

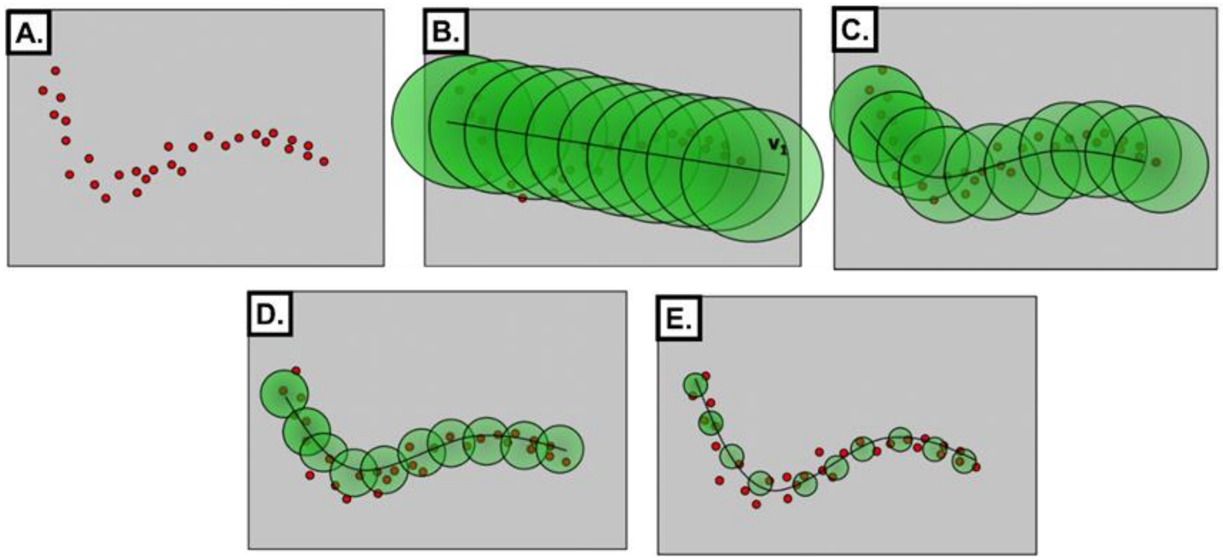

Figure 1-6. Application of Gaussian probability density functions for GTM, A) data in 2D space, B) Gaussian centers defined falling along the first eigenvector (iteration 1), C) Gaussians shrink and the manifold deforms, the centers are moving to fit the data (iteration 2), D) process continues deforming the manifold (iteration 3), and E) expectation can no longer be maximized by any further deformation (modified from AASPI documentation).

GTM is a non-linear dimensionality reduction technique that uses optimized Gaussian mixture models to allow for a more probabilistic representation of the data in a lower dimensional space (Bishop et al. 1998; Roy et al. 2014). In contrast to the SOM, GTM transforms regularly spaced grid points from the 2D latent space into the N-dimensional space by using non-linear functions, a vector will represent the initial grid point inside the now called non-Euclidian manifold, and a probability density function (PDF) of representing a data vector will be centered in each vector. During the training process, and using optimization EM-algorithms, the PDFs will change to better represent the data, and the final model will be projected back to the latent space by using Bayes' theorem (Bishop et al. 1998). Clustering will be made by assigning a 2D color scale, and like SOM, features with similar colors can be associated with similar nature.

A schematic representation is shown in Figure 1-6 for a 1-dimensional curve example from Bishop (1998). Data is plotted in a 2D space (Figure 1-6A), the projected latent points will fall along the corresponding first eigenvector, and a PDF centered on each point will be assigned (Figure 1-6B). Through several iterations (Figure 1-6C, D, E), the Gaussian functions will accommodate to better represent the data.

RESULTS

Multiattribute Analysis

The results of the multiattribute analysis are presented in Figure 1-7 and Figure 1-8, and they are shown as seismic attribute extractions over three horizons near the zones of interest inside the Duperow formation: Upper Duperow, Mid-Duperow, and Lower Duperow. The length of the search window was specified as zero to ensure that the values over the surface extractions are those of the surface picked and are not affected by other attribute values above or below it.

Broadband and multispectral coherence results are shown in Figures 1-7A and 7B respectively. Notice that the features seen in the coherence attribute are unclear and it is not possible to tell whether they are structural or stratigraphically related (white arrows, Figure 1-7A). With the multispectral coherence approach though, features with a NW-SE trend (cyan arrows, Figure 1-7B) become more obvious in all three horizons and some smaller features with NE-SW trend appear on the near Upper and Mid-Duperow (green arrows, Figure 1-7B). However, the target faults F1, F2, and F3, observed below the Duperow Formation in the amplitude volume, remain absent.

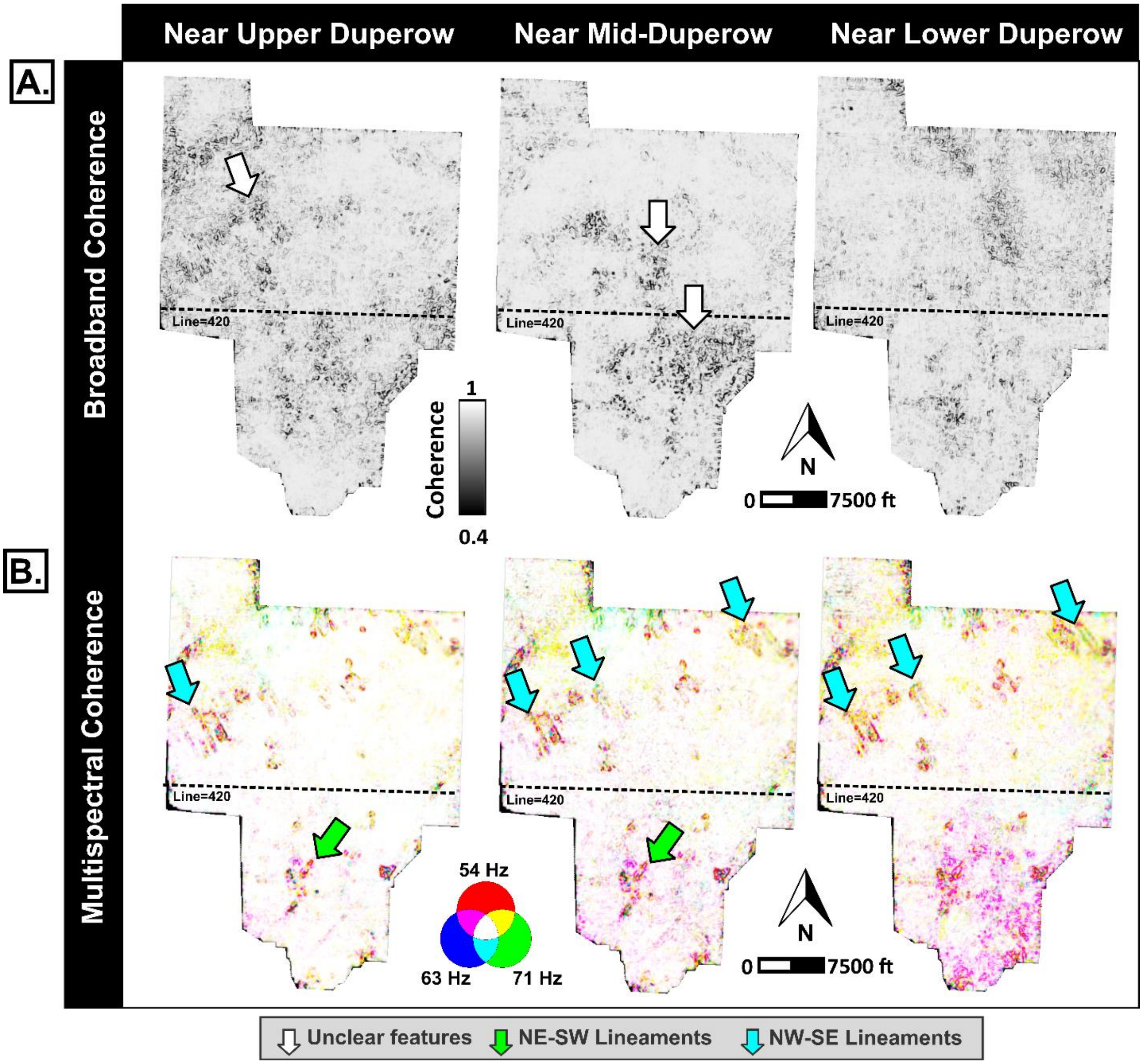

Figure 1-7. Surface extractions over the horizons of interest for A) broadband coherence and B) multispectral coherence, as an RGB blend of the three selected frequencies.

Curvature attributes give a better idea of the features with NW-SE and NE-SW trends (cyan and green arrows, Figure 1-8A). Notice they have a negative curvature response surrounded by a positive curvature response, similar to an elongated bowl-like shape feature. We can see these patterns mainly in the northwest zone near the Upper and Mid-Duperow horizons. Moreover, curvature attributes highlight one of the main faults (F1) in the three horizons of interest, notice it is characterized by a positive to the west and negative to the east response (yellow arrow, Figure 1-8B). In the Lower and Mid-Duperow, a second NS pattern is seen, probably related to a second main fault (yellow arrow, F3).

Figure 1-8B shows the results obtained with aberrancy attributes. Aberrancy succeeds in mapping all three main faults with NS trend (yellow arrows) in the three horizons and it highlights other lineaments with NE-SW trend (green arrows), not previously seen with the more conventional attributes. Besides this, the features with NW-SE trend (cyan arrows) in the northwest and northeast of the near Upper and Mid-Duperow are more clearly distinguished than in the previous curvature attribute, and it is possible to notice a parallel geometric pattern with the other NW-SE trends and an almost 60° difference from the NE-SW lineaments.

Moreover, aberrancy is able to provide us with another level of detail. When looking at the azimuths associated with each pattern, we can see that NE-SW features have a double signature of green and magenta colors (approximately 60° and -120°, respectively, in the color bar) while NW-SE features have a double signature of cyan and red colors (approximately 120° and -60°, respectively). The main faults though, seem to have a single response of light green color (approximately 90°). These degree values indicate the direction of flexure. In that sense, we see two flexure values when we have bowl-like shape features, first flexure when it changes from positive to negative and second flexure when it changes from negative to positive, and a single flexure when we only have the bend associated with a fault.

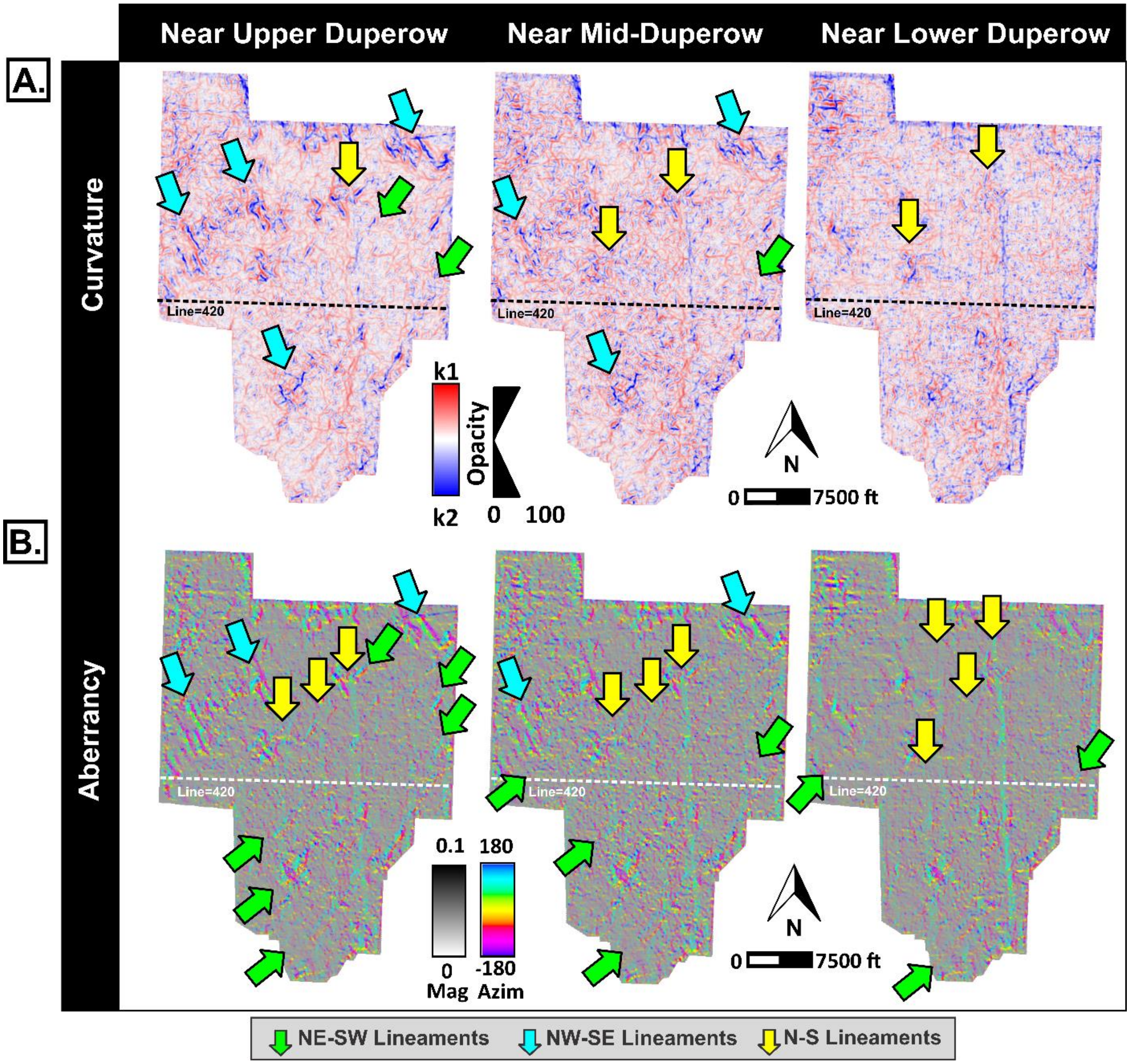

Figure 1-8. Surface extractions over the horizons of interest for A) curvature, as a co-render of the k1-most positive curvature and k2-most negative curvature, and B) total aberrancy, as a co-render of total aberrancy magnitude and total aberrancy azimuth.

This extracted information from the multiattribute analysis, particularly the aberrancy attributes, serves two purposes. First, it complements the data obtained from curvature attributes by pinpointing the precise location of flexure, which could signify faulting if we later confirm that these lineaments are structurally related. Secondly, it would enhance the visualization of seismic lineaments, especially those associated with discontinuities with offsets below seismic resolution. This is different from curvature attributes, which primarily provide information about the adjacent sides of the flexure. In this way, we can effectively map the location of sub-seismic faults that may have been overlooked when using conventional seismic attributes like broadband and multispectral coherence.

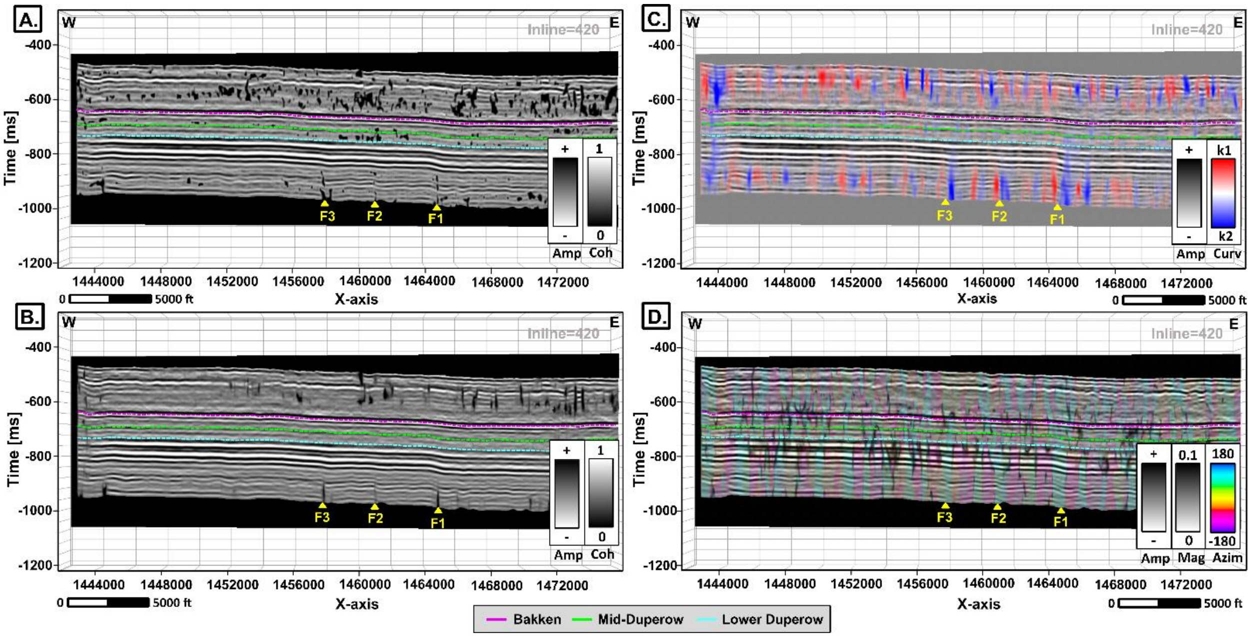

Figure 1-9. Inline 420 showing the co-render of the seismic amplitude volume and the seismic attribute response in the vertical component: A) broadband coherence, B) multispectral coherence bandlimited to 54-63-71 Hz, C) curvature (k1-most positive and k2-most negative, and D) aberrancy (azimuth and magnitude).

Finally, to visualize these seismic attribute responses over the seismic amplitude volume, their co-renders have been displayed as vertical sections in Figure 1-9. Notice how the faults F1, F2, and F3 from Figure 1-2 are clearly highlighted in the reflectors below target with the broadband (Figure 1-9A) and multispectral (Figure 1-9B) coherence, but within the zone of interest (Duperow Formation) there is no clear response. With the coherence attribute, we can see the uncorrelated noise in the Mid-Duperow, but the multispectral coherence helps remove it while sharpening the fault expression in the deeper reflectors. In Figure 1-9C, the positive (upthrown side) and negative (downthrown side) responses associated with each side of the faults can be seen in the curvature attribute. When looking at the results obtained with aberrancy attributes in Figure 1-9D, we can see these attributes provide much more information within the intervals of interest than the previous seismic attributes, as they highlighted both the magnitude and azimuth of the flexure. Observe again that the main faults are highlighted with light green colors in the azimuth attribute, which will indicate a flexure towards the east.

Machine Learning

Figure 1-10 and Figure 1-11 show the results obtained when integrating the different geometric seismic attributes using SOM and GTM, respectively. Similar to the multiattribute analysis, results are presented as attribute extractions with zero-length window over the horizons within the target zone of the Duperow Formation.

SOM 1 and SOM 2

Figure 1-10A shows the surface extractions over the SOM1 when integrating all the geometric seismic attributes while Figure 1-10B shows the results for the SOM2 when integrating only curvature and multispectral coherence attributes.

Notice that in Figure 1-10A and B, each cluster (color) of the SOM seems to be associated with a seismic attribute, which in turn means it will be associated with the specific type of fault expression highlighted by each of them as seen in Figure 1-4. Purple clusters highlight the features marked by the multispectral and broadband coherence, therefore, where there is a discontinuity of the reflector; while orange clusters and green clusters highlight k1-most positive and k2-most negative curvature, respectively, what would indicate the upthrown side and downthrown side of the fault, if lineaments are found to be structurally related.

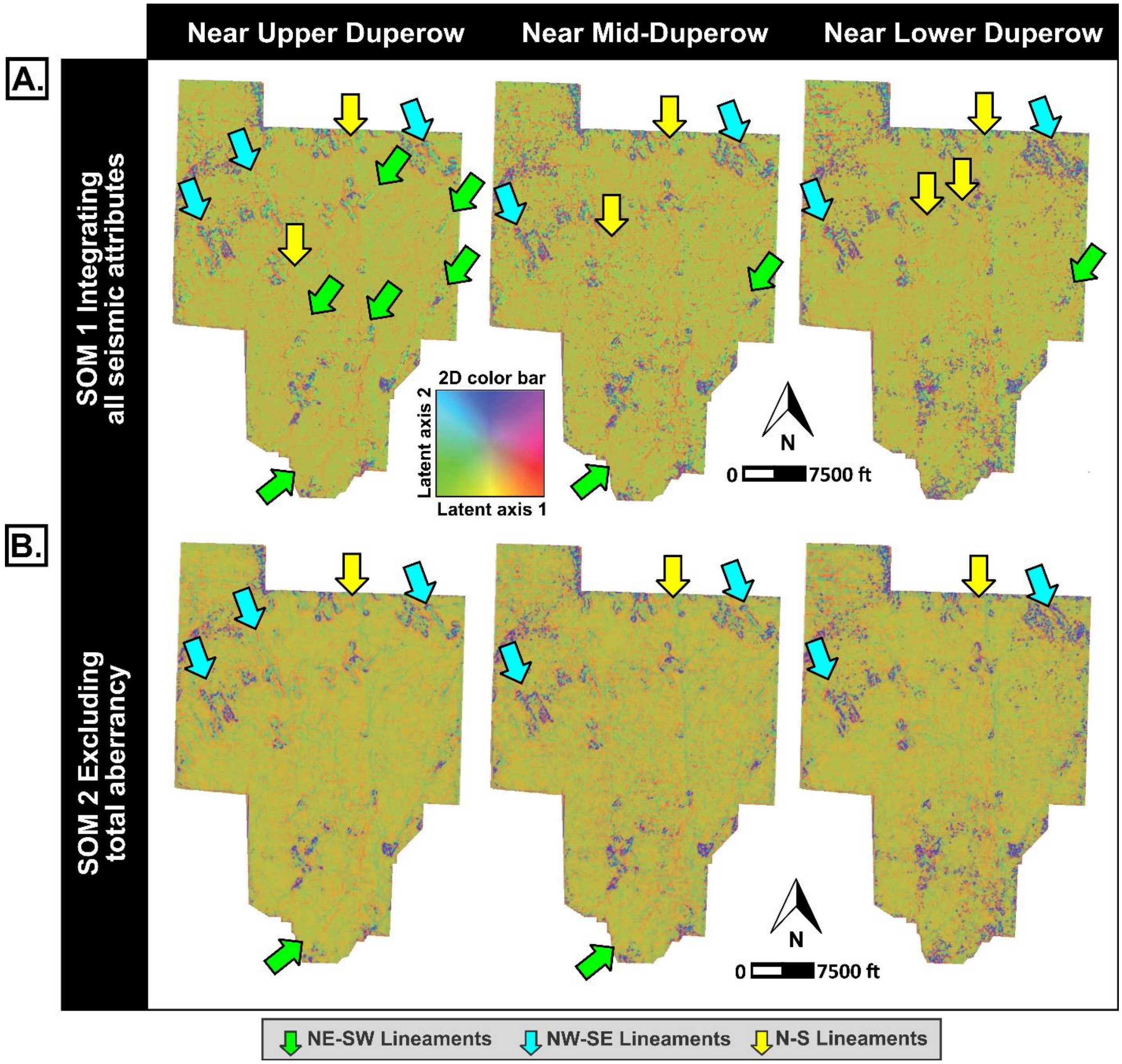

Figure 1-10. Surface extractions over the horizons of interest for A) SOM 1 calculated integrating: broadband coherence, multispectral coherence (54, 63, and 71 Hz), curvature (k1 and k2), and aberrancy (magnitude and azimuth), and B) SOM 2 calculated integrating only broadband coherence, curvature (k1 and k2) and multispectral coherence (54, 63, and 71 Hz).

One may say that this would not be much different than an image created by the co-render of coherence and curvature attributes. However, notice that in Figure 1-10A, there is a higher level of contrast between the different features, which makes the subtler features more noticeable. This contrast seems to be provided by the inclusion of aberrancy attributes, as is the only parameter changing between each SOM scenario run. In other words, when comparing the SOM results when including (SOM 1) and excluding (SOM 2) aberrancy attributes, we can clearly see that SOM 1 shows a better visualization of the different lineaments, especially those detected only by the aberrancy attributes in the multiattribute analysis step. Also, notice that the contrast for the main NS fault to the east (F1) is much clearer in SOM1 than in SOM 2.

GTM 1 and GTM 2

Similar observations can be made for the GTM results (Figure 1-11A and B). First, we can see that different clusters are being assigned to a specific seismic attribute, and therefore, fault expression associated; dark purple corresponds to broadband and multispectral coherence, while orange and light blue correspond to k1-most positive and k2-most negative curvature, respectively. However, we see that geometric pattern and, in general, lineaments mapping is easier over the volume that integrates aberrancy attributes and not only conventional attributes.

GTM 1 provides a much better image in which all lineaments can be mapped. Notice that besides being able to more easily visualize NE-SW and NW-SE lineaments (green and cyan arrows, respectively), the contrast provided for the F1, F2, and F3 is outstanding (yellow arrows) if compared with any of the results observed in the multiattribute analysis and the SOM itself. In GTM 2 (and also in SOM 2), when excluding aberrancy attributes, only the N-S fault seen is F1, however, GTM 1 is able to capture the three of them. GTM 2 provides a less-quality image where, despite being possible to see coherent patterns in the NW-SE, SE-NW, and N-S directions, it is more difficult to define exactly where the possible faults would go.

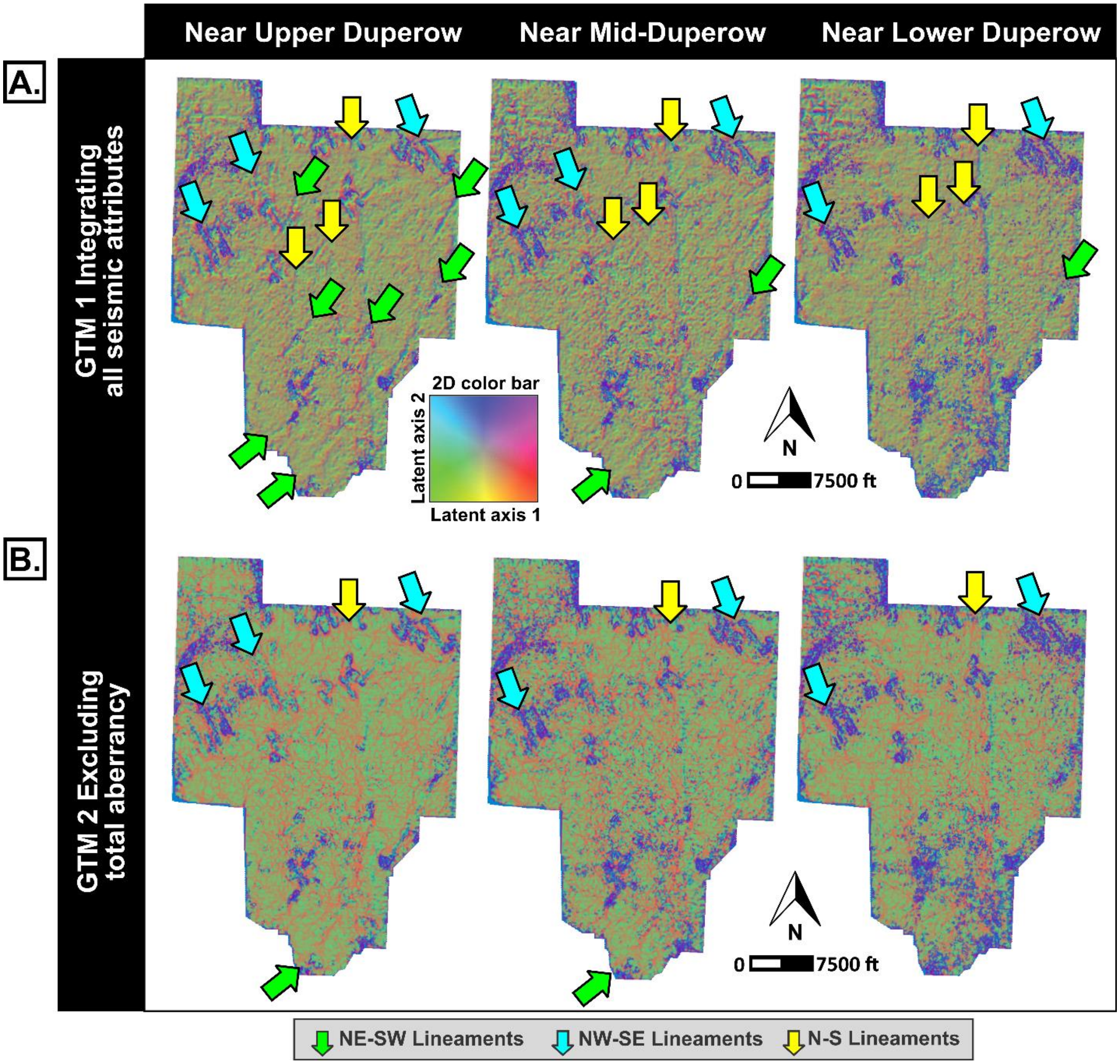

Figure 1-11. Surface extractions over the horizons of interest for A) GTM 1 calculated integrating: broadband coherence, multispectral coherence (54, 63, and 71 Hz), curvature (k1 and k2), and aberrancy (magnitude and azimuth), B) GTM 2 calculated integrating only broadband coherence, curvature (k1 and k2) and multispectral coherence (54, 63, and 71 Hz).

SOM vs GTM

Another noteworthy observation is that when comparing SOM and GTM, the results provided by GTM (Figure 1-11A and B) seem to facilitate the visualization of lineaments more easily than those provided by the SOM (Figure 1-10A and B). If comparing SOM1 with GTM1, which are the best images obtained for each method, we can see that the clustering made by the GTM is able to better integrate all the details provided by each individual seismic attribute into a single volume that enhance the visualization of all different geological features. Even when comparing the results of SOM2 with GTM2, the GTM method provides a better contrast between all different clusters.

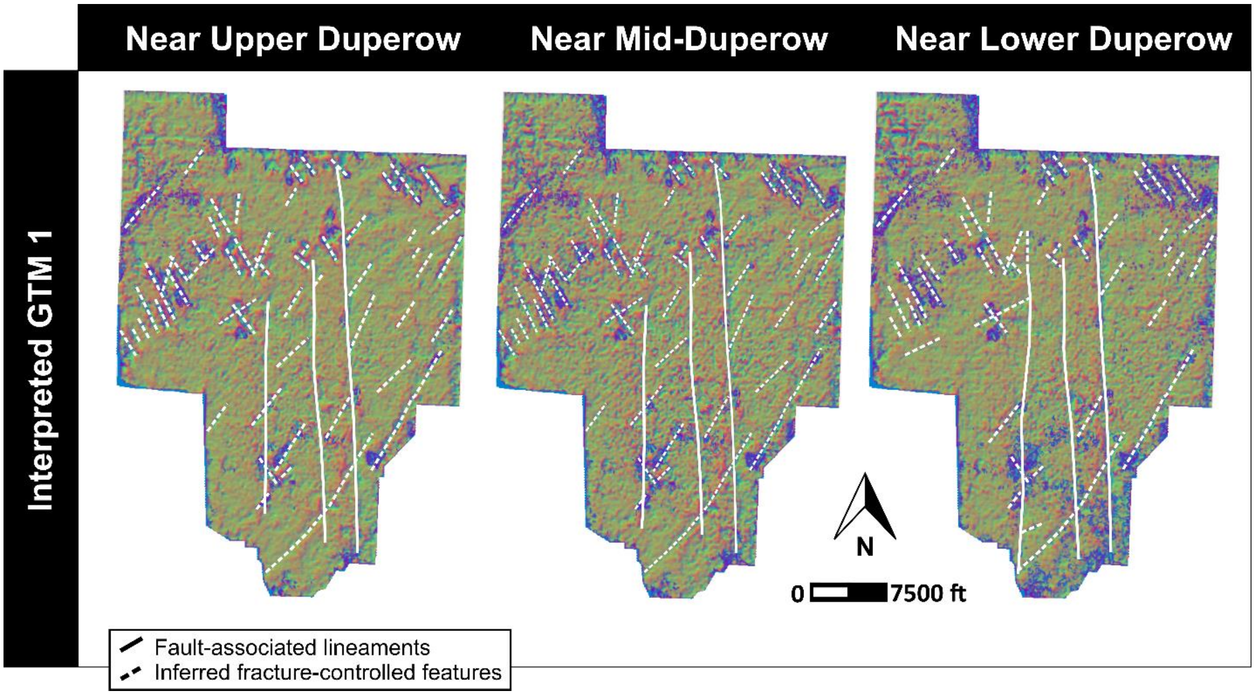

Figure 1-12. Lineaments interpretation in the horizons of interest over the GTM 1 results.

Figure 1-12 shows an interpretation of the surface extractions of the best-case scenario obtained, which was GTM 1. Notice that we are not only able to map the initial target N-S faults F1, F2, and F3 (solid lines) but also the different lineament types in the NE-SW and NW-SE directions (dashed lines). Notice there is a clear geometric pattern among the different lineaments mapped, which may indicate fracture control.

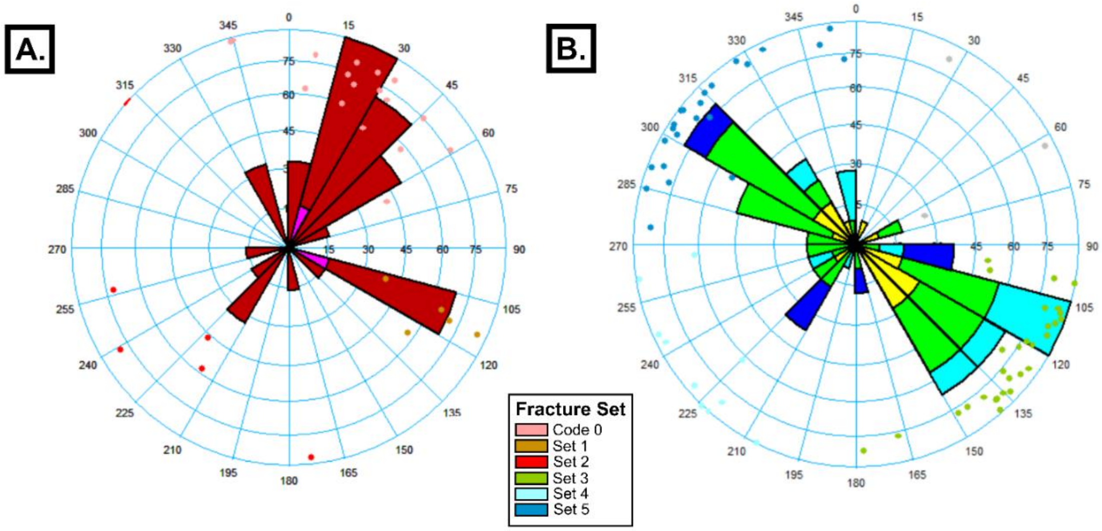

Figure 1-13. A) Fracture group 1 reported in the Nisku and Potlach formations, B) fracture group 2 reported in upper, middle, and intermediate Duperow (modified from Zaluski, 2018). Different colors represent different fracture sets.

DISCUSSION

A question that arises is whether these subtle features observed in the seismic data are stratigraphically or structurally related. From the curvature response, we could infer they are stratigraphic, more specifically, karstic related. However, the clear geometric pattern seen between the NW-SE and NE-SW trends in the aberrancy attributes and ML results may lead us to infer there is a structural control associated and, therefore, potential sub-seismic faulting in these directions.

Figure 1-13 shows two rose diagrams created from FMI log data of the Danielson 33-17 and Wallewein 22-1 wells and presented in the report of Zaluski (2018). By being a naturally fractured reservoir, we would not expect to see any of the fractures of the Duperow Formation on the seismic data. However, and despite the difference in scale between seismic and well data, we can see there is a clear similarity between the strikes of the lineaments mapped with seismic-derived data (Figure 1-12) and those observed in the fracture sets detected with FMI logs (Figure 1-13).

Fracture group 1 (NE-SW strike) is mainly present in the upper part near the Nisku and Potlach formation, while fracture group 2 (NW-SE) is more prominent in the Duperow Formation (Zaluski, 2018). A similar pattern can be observed in the attribute and ML-assisted seismic interpretation, NE-SW lineaments are more obvious near Upper Duperow while NW-SE features are more easily seen in all the three horizons inside the Duperow Formation (Upper, Mid-, and Lower).

In that sense and using the well data as a proxy and the only information available to get an insight into the planes of favorable weakness inside the formation of interest, we can confirm that our observations in the seismic data make geological sense and may have a structural component. More specifically, we could infer that the features observed may indeed be stratigraphic features structurally controlled and developed in those NE-SE and NW-SE directions of favorable weakness in the rock.

The detection of this sub-seismic faulting can be crucial for any project aiming to inject fluids in a reservoir. This information further obtained from the inclusion of the aberrancy attributes in the multiattribute analysis and ML steps can be of great help to interpreters to better characterize reservoirs and understand the structural components of a target formation.

Further studies should explore statistical measurements of improvement comparison between discontinuity detection using conventional methods versus more novel methods such as the aberrancy attributes. Moreover, automatic extraction of potential fault planes from both the aberrancy attributes volumes and the ML results could be explored.

CONCLUSIONS

Seismic attributes such as broadband and multispectral coherence, and curvature, are some of the most common, if not the most, geometric attributes implemented by seismic interpreters to aid in structural interpretation. However, the inherent restrictions of seismic data resolution and the mathematical background of these attributes limit the amount of information that can be extracted from the seismic.

In this study, we saw that broadband coherence and multispectral coherence, by being discontinuity-based attributes, failed in the scenarios where fault expression did not have a clear break in the seismic reflector. Curvature attributes, by being related to the fold of the reflector, were able to provide us with more information about the lineaments seen, indicating an elongated bowl-like shape for those with NE-SW and NW-SE trends, and that we inferred could be stratigraphically related but structurally controlled.

We also showed that aberrancy attributes, by being related to the flexure of the reflector, were more sensitive to smaller perturbations of the reflector structure, therefore, allowing us to better visualize lineaments in the seismic that could potentially be related to faults with sub-seismic vertical displacement. In this study, aberrancy attributes helped enhance the visualization of both the reported NS faults, and potential faults with NW-SE and NE-SW strike, similar to the strikes seen with well log data for fractures inside the target interval. This NS, NW-SE, and NE-SW faulting was mostly missed by the conventional seismic attributes of broadband and multispectral coherence, and curvature.

Nevertheless, it is important to recognize that adding another seismic attribute, such as aberrancy, to the list of recommended attributes for common multiattribute analysis workflows also increases the time spent by the interpreter. Here, we have shown how it is possible to integrate all geometric seismic attributes in a way they can all contribute to have an image that highlight faults with different expressions in the seismic, from those with clear reflector discontinuity to those seen as subtle flexures of the reflector.

Here, we tested SOM and GTM methods when using geometric attributes as input for the clustering process. We demonstrated that when integrating aberrancy attributes along with broadband and multispectral coherence, and curvature, the visualization of lineaments was considerably uplifted in comparison with the cases where they were excluded from the input attribute list, or even when interpreting in the individual attribute volumes during the multiattribute analysis stage. We also showed that from the ML methods tested, GTM showed better visualization results than SOM.

In that sense, for interpreters working on structural interpretation, whether interested on focusing on multiattribute analysis only or applying ML methods, such as those presented here, we highly encourage making a common practice to include aberrancy attributes along with other common geometric seismic attributes. This will provide another level of detail of which seismic interpreters can considerably benefit from as more information can be enhanced that would allow for a better understanding of a structural setting, especially when information such as well logs are not available.

ACKNOWLEDGEMENT

The authors would like to thank the sponsors of the Attribute Assisted Seismic Processing and Interpretation Consortium (AASPI) and Schlumberger for providing the software used in this study, the Department of Energy for the seismic and well log data, and Zanskar Geothermal & Minerals Inc.

REFERENCES

Bahorich, M. and S. Farmer, 1995, 3-D seismic discontinuity for faults and stratigraphic features: The coherence cube: The leading edge, 14 (10), 1053– 1058.

Bedle, H., D. Salazar Florez, and C. R. H. Garneau, 2022, Recognizing societal influences in earthquake geohazard risk perception with explainable AI while mitigating risks through improved seismic interpretation: The Leading Edge, 41 (11), 756–767.

Bhattacharya, S. and S. Verma, 2019, Application of volumetric seismic attributes for complex fault network characterization on the North Slope, Alaska: Journal of Natural Gas Science and Engineering, 65, 56–67.

Bishop, C. M., M. Svensen, and C. K. I. Williams, 1998, The generative topographic mapping: Neural Computation, 10, 215–234.

Chopra, S., and K. J. Marfurt, 2007, Curvature attribute applications to 3D surface seismic data: The Leading Edge, 26 (4), 404-414.

Chopra, S., and K. J. Marfurt, 2011, Interesting pursuits in seismic curvature attribute analysis: CSEG Recorder, 36, 40 – 50.

Chopra, S., and K. J. Marfurt, 2018, Seismic facies classification using some unsupervised machine-learning methods: 88th Annual International Meeting, SEG, Expanded Abstracts, 2056–2060.

Chopra, S., and K. J. Marfurt, 2020, Adopting multispectral dip components for coherence and curvature attribute computations: The Leading Edge, 39 (8), 593-596.

Clochard, V., B. Devault, D. Bowen, N. Delépine, and K. Wangkawong, 2018, Quadri-joint inversion: Method and application to the Big Sky 9C 3D data set in northern Montana: Interpretation, 6(4), SN101-SN118.

Ellsworth, W. L., 2013, Injection-Induced Earthquakes: Science, 341, 1225942.

Gao, D., 2013, Integrating 3D seismic curvature and curvature gradient attributes for fracture characterization: Methodologies and interpretational implications: Geophysics, 78, O21 – 031.

Falconer S. and K. J. Marfurt, 2008, Attribute-driven footprint suppression: SEG Technical Program Expanded Abstracts, 2667-2671.Fehmers, G. C., and C. F. W. Höcker, 2003, Fast structural interpretation with structure-oriented filtering: Geophysics, 68 (4), 1286–1293, doi: 10.1190/1.1598121

Gao, D., and H. Di, 2015, Extreme curvature and extreme flexure analysis for fracture characterization from 3D seismic data: New analytical algorithms and geologic implications: Geophysics, 8, IM11– IM20.

Guo, H., K. J. Marfurt, and J. Liu, 2009, Principal component spectral analysis: Geophysics, 74 (4), P35–P43.

Gupta, N., S. Sarkar, K. J. Marfurt, 2013, Seismic attribute driven integrated characterization of the Woodford Shale in west-central Oklahoma: Interpretation, 1 (2), SB85–SB96.

Hussein M., R. R. Stewart, and J. Wu, 2021, Which seismic attributes are best for subtle fault detection?: Interpretation, 9 (2), T299–T314.

Karam, P., S. Mitra, K. Marfurt, and B. M. Carpenter, 2021, Synthetic transfer zone characterization using seismic attributes: An example from the Parihaka fault system in the Taranaki Basin, New Zealand, Interpretation, 9 (3), T653–T665.

Kay, E. A., D. A., Bodnar, and E. C. Cazier1993, Faulting: A Major Control on Fluid Flow and Production Performance, Prudhoe Bay Field, Alaska: SPE Western Regional Meeting, Anchorage, Alaska.

Kohonen, T., 1982, Self-organized formation of topologically correct feature maps: Biological Cybernetics, 43, 59–69.

Li, F., J. Qi, B. Lyu, and K. J. Marfurt, 2018, Multispectral coherence: Interpretation, 6, T61 – T69.

Libak A., B. Alaei, and A. Torabi, 2017, Fault visualization and identification in fault seismic attribute volumes: Implications for fault geometric characterization: Interpretation, 5 (2), B1–B16.

Lubo Robles, D., H. Bedle, K.J. Marfurt, and M.J. Pranter, 2023, Evaluation of principal component analysis for seismic attribute selection and self-organizing maps for seismic facies discrimination in the presence of gas hydrates: Marine and Petroleum Geology, 150, 106907.

Luo, Y., M. Marhoon, S. Al Dossary, and M. Alfaraj, 2002, Edge-preserving smoothing and applications: The Leading Edge, 21 (2), 136–158.

Lyu, B., J. Qi, F. Li, Y. Hu, T. Zhao, S. Verma, and K. J. Marfurt, 2020, Multispectral coherence: Which decomposition should we use?: Interpretation, 8, T115–T129.

Maas, M.V.R., H. Bedle, and M. C. Matos, 2023, Seismic identification of carbonate reservoir sweet spots using unsupervised machine learning: A case study from Brazil deep water Aptian pre-salt data: Marine and Petroleum Geology, 151, 106199.

Onishi T., M. Nguyen, J. Carey, B. Will, W. Zaluski, D. Bowen, B. Devault, A Duguid, Q. Zhou, S. Fairweather, L. Spangler, and P. Stauffer, 2019, Potential CO2 and brine leakage through wellbore pathways for geologic CO2 sequestration using the National Risk Assessment Partnership tools: International Journal of Greenhouse Gas Control, 81, 44–65.

Patel, S., F. Kolawole, J. I. Walter, X. Chen, and K. J. Marfurt, 2021, Seismic illumination of small-throw seismogenic faults, Anadarko Basin, Oklahoma: Interpretation, 9, SE35–SE5.

Qi, X., and K. J. Marfurt, 2018, Volumetric aberrancy to map subtle faults and flexures: Interpretation, 6, T349–T365.

Roy, A., K. J. Marfurt, and M. C. Matos, 2011, Application of 3D clustering analysis for deep water marine Seismic facies classification-an example from deep water Northern Gulf of Mexico: GCSSEPM, 410–441.

Roy A, A. Romero-Peláez, T. Kwiatkowski, K. Marfurt, 2014, Generative topographic mapping for seismic facies estimation of a carbonate wash, Veracruz Basin, southern Mexico: Interpretation, 2(1), SA31–SA47.

Schneider, S., C. G. Eichkitz, M. G. Schreilechner, and J. C. Davis, 2016, Interpretation of fractured zones using seismic attributes—Case study from Teapot Dome, Wyoming, USA: Interpretation, 4 (2), T249–T260.

Zaluski, W., 2018, Kevin Dome static model development final report: Schlumberger Carbon Services, Sky Carbon Sequestration Partnership.

Zhao, T., V. Jayaram, A. Roy, and K. J. Marfurt, 2015b, A comparison of classification techniques for seismic facies recognition: Interpretation, 3 (4), SAE29–SAE58.

CHAPTER 2. REVEALING THE HIDDEN FAULTS OF THE OKLAHOMA BASEMENT THROUGH UNSUPERVISED MACHINE LEARNING AND INTEGRATION WITH EARTHQUAKE DATA

ABSTRACT

Oklahoma has recently drawn a lot of interest due to its increase in induced seismicity, which has been associated with the injection of wastewater in the sedimentary strata overlying the basement. Most of these seismogenic faults were unmapped and not present in the Oklahoma Geological Survey fault database before their reactivation. However, correctly knowing fault orientation and geometry, as well as the local stress fields are crucial to evaluate the reactivation potential of a fault, and therefore the potential seismicity hazard associated. Here, different geometric seismic attributes were analyzed and integrated using unsupervised machine learning to identify potential basement-rooted faults and strike-slip-related structures. The machine learning results not only confirmed the existence of NE-SW faults that extend from the basement upward into the sedimentary section and that correlated with earthquake data but also the potential existence of other NE-SW structurally controlled features of anticlinorium shape.

INTRODUCTION

The increase of seismicity in Oklahoma associated with the increase of wastewater injection has awakened a great interest among the scientific community to map and understand the fault structures that could be stressed to the point of rupture. These faults have been reported to be at basement depth and their existence has been revealed only by the recent earthquake events. In that sense, the current case in Oklahoma has clearly demonstrated that failing to map faults, no matter the stratigraphic level, could not only become a potential geohazard for the communities but also jeopardize the societal perception of the energy industry techniques (Bedle et al. 2022).

Most recently, different approaches have been applied for mapping and understanding basement faults in Oklahoma, including studies focused on earthquake data (Chen et al. 2017; Skoumal et al. 2019; Qin et al. 2019), core data (Hamilton et al., 2021), seismic attributes analysis over the sedimentary strata immediately overlaying the basement (Kolawole et al. 2019; Kolawole et al. 2020, Firkins et al. 2020; Patel et al. 2021), and aeromagnetic data (Chase et al. 2022; Elebiju et al. 2011). By using seismic reflection data, Kolawole et al. (2019, 2020) and Firkins et al. (2020) focused on coherence and curvature attributes while Patel et al. (2021) focused on curvature, coherence, and aberrancy. All of them have obtained promising results by integrating seismic attributes and confirming observations with earthquake data, demonstrating that it is possible to expand our knowledge on basement faults in Oklahoma with these types of approaches, despite the chaotic seismic facies associated with crystalline rocks.

Another approach not yet tested is the integration of all the different types of seismic attributes through machine learning (ML) techniques. In this study, a 3D seismic dataset is used to explore the applicability of unsupervised ML methods for the identification of faults in the basement of Oklahoma. The observations are compared with available earthquake data in the area, which have already confirmed the presence of faults in the basement underlying the study area. If the ML methods appeared to be successful in the identification of basement faults through the integration of seismic attributes, this approach could be further expanded to other seismic datasets in the area and help to improve the knowledge on the structural geology of Oklahoma.

Dataset

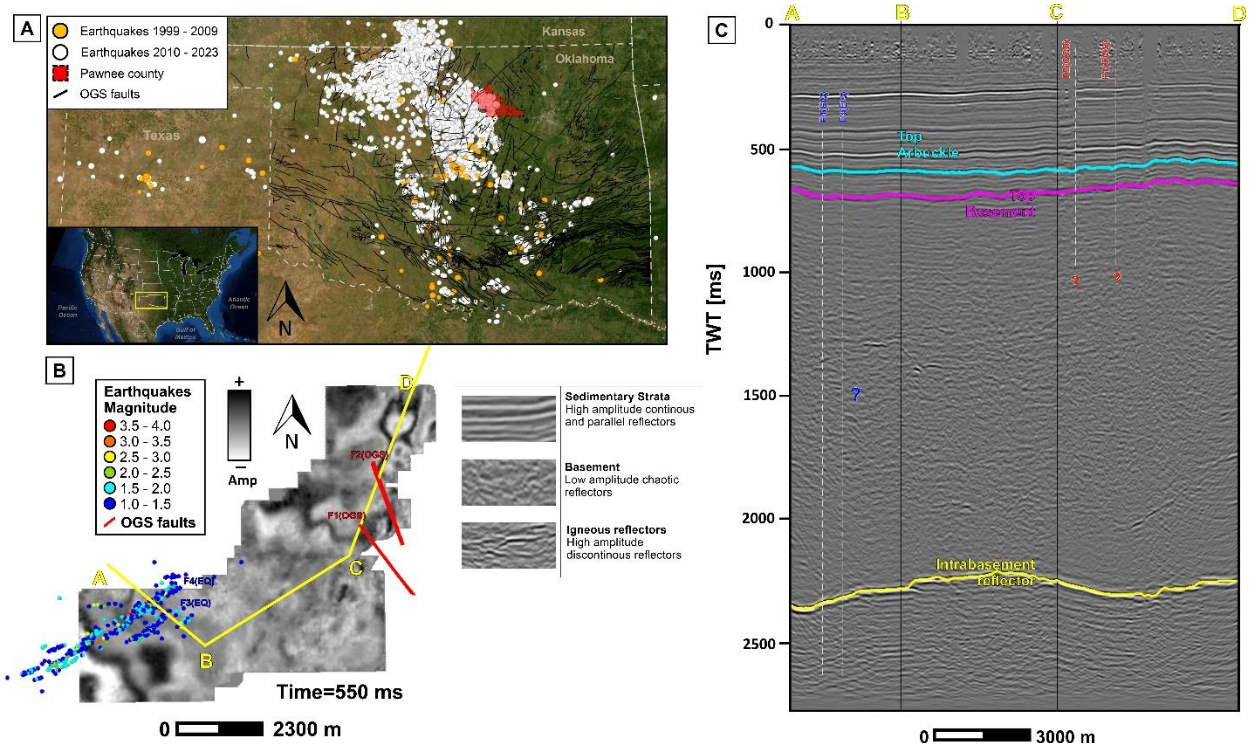

Figure 2-1. A) Oklahoma structural map reported by the OGS and earthquake data from the USGS, B) time slice at 550 ms showing the location of the earthquake data from Park et al. (2022), the faults from the OGS, and seismic facies identified in the area, and C) cross section indicating the three main horizons of interest: top of the Arbuckle formation, top of the basement, and the intrabasement reflector.

The 3D seismic dataset used for this study is located in Pawnee County, in the northern part of Oklahoma, and within the Cherokee Platform geological province (Figure 2-1A). It covers an approximate area of 44.6 square km, has a record length of 2.8 s, a sample rate of 0.002 s, and a bin size of 33.5 by 33.5 m. On the other hand, the earthquake dataset was obtained from Park et al. (2022) and is comprised of 594 events recorded between May 2014 and June 2019.

The seismic characteristics of this dataset are rather straightforward. Parallel reflectors are associated with the sedimentary strata and chaotic reflectors are associated with the crystalline rocks that conform the basement. Besides the folding of the parallel reflectors, there is no other feature, such as obvious discontinuities, that can suggest faulting in the area, and the only information that confirms, so far, the existence of basement faulting comes from the earthquake data (Figure 2-1B).

An interesting feature seen in the dataset is a continuous reflector within the basement interval, here called intrabasement reflector (IBR) for simplicity (Figure 2-1C). This reflector extends over the entire area and will help to correlate observations seen within the upper sedimentary strata and those associated with intervals at basement depth.

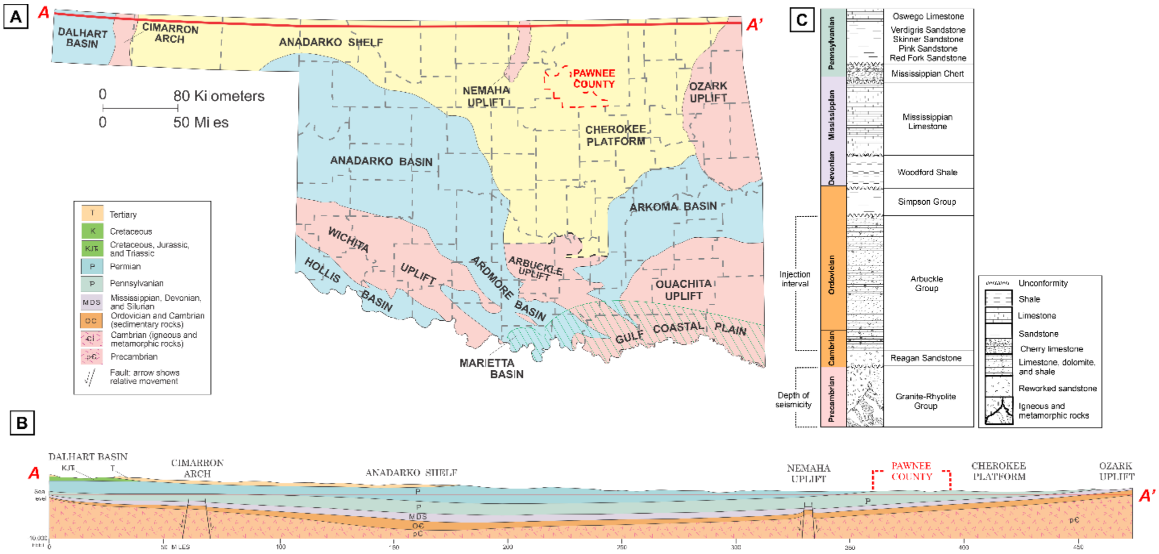

Figure 2-2. A) Map of the geological provinces of Oklahoma, B) cross-section A-A' indicating the location of Pawnee County (modified from Johnson, 2008), and C) stratigraphic column for northcentral Oklahoma indicating the interval of wastewater injection and depth of seismicity (modified from Elebiju et al. 2011).

Geological Setting

Located in northeastern Oklahoma, the Cherokee Platform province has been considered a relatively stable platform when compared to the adjacent Anadarko and Arkoma Basins to the south and southwest in Oklahoma and Arkansas, where many major tectonic events occurred and the sedimentary section is much thicker (Drake and Hatch, 2020; Figure 2-2). Interestingly, the Oklahoma basement was generally assumed to be a tectonically stable basement until the increase in seismic activity revealed the reactivation of pre-existent basement faults.

The Oklahoma basement is part of the Southern Granite Rhyolite Province of the Central United States and is considered to have formed about 1400 - 1340 Ma (Bickford et al., 2015). In the northeastern region, Denison (1981) classified these rocks into four units: Washington Volcanic Group, Spavinaw Granite Group, Osage Microgranite, and the Central Oklahoma Granite Group, of which the first three comprised the Northeast Oklahoma Province. The study area is underlain by the Washington Volcanic Group, which Denison (1981) describes as composed mainly of rhyolite with certain areas of andesite.

Some main differences between the Northeast Oklahoma Province and the Wichita Province in the south were indicated by Denison (1981) as being the lack of diabase dikes and sills in northeastern Oklahoma, which are exceptionally common in the Wichita Province. Moreover, besides the granite and rhyolite, layered gabbroic mass and basalt spilite sequences are also present in the southern part (Denison 1981; Hames et al., 1997; Hogan et al., 1997; Hogan and Gilbert, 1997). These gabbro and basaltic dikes in the Wichita Province are associated with the formation of the Southern Oklahoma Aulacogen, which developed during the rifting of the Laurentian Supercontinent in Late Proterozoic to Cambrian time and was accompanied by bimodal igneous activity (Hogan and Gilbert, 1997).

Different studies focused on seismic reflection data covering the northern regions of Oklahoma have consistently reported distinct reflectors within the basement intervals and are referred to as intrabasement reflectors. Elebiju et al. (2011) and Kolawole et al. (2020) reported a characteristic reflection pattern of trough-peak-trough, associated to an increase in acoustic impedance, and suggested it is related to a change from a more felsic rock, such as those of the granite-rhyolite province, to a higher impedance rock, such as a mafic intrusion. Besides helping to expand on the knowledge of the tectonic history of the basement in Oklahoma, these intrabasement reflectors are of interest because they can help understanding intrabasement deformation, and later reactivation and propagation up into the sedimentary cover, which will help explain fault connectivity and potential fluid migration pathways from the sedimentary strata to the basement and the relationship with current seismicity in northcentral Oklahoma (Kolawole et al., 2020).

METHODS

The methods implemented in this study for the structural interpretation of basement-rooted faults cover conventional seismic mapping, seismic attributes, assisted interpretation through application of ML techniques, and seismic time-to-depth conversion. The generalized workflow is presented in Figure 2-3.

During the data conditioning step, we applied a structure-oriented filter, which is intended to attenuate random noise and enhance the edges of structures (Luo et al. 2002; Fehmers and Höcker, 2003). Using conventional mapping strategies, we continued to map the horizons of interest, so that we could make our interpretations using surface extractions. We then proceeded with the calculation of the selected seismic attributes, broadband coherence, multispectral coherence, curvature, and aberrancy, and their integration using self-organizing maps (SOM) and generative topographic mapping (GTM). Finally, we converted all seismic inputs and outputs to depth to be able to compare our structural interpretations with the earthquake data in the same domain as well as calculate dip and strikes of the faults interpreted.

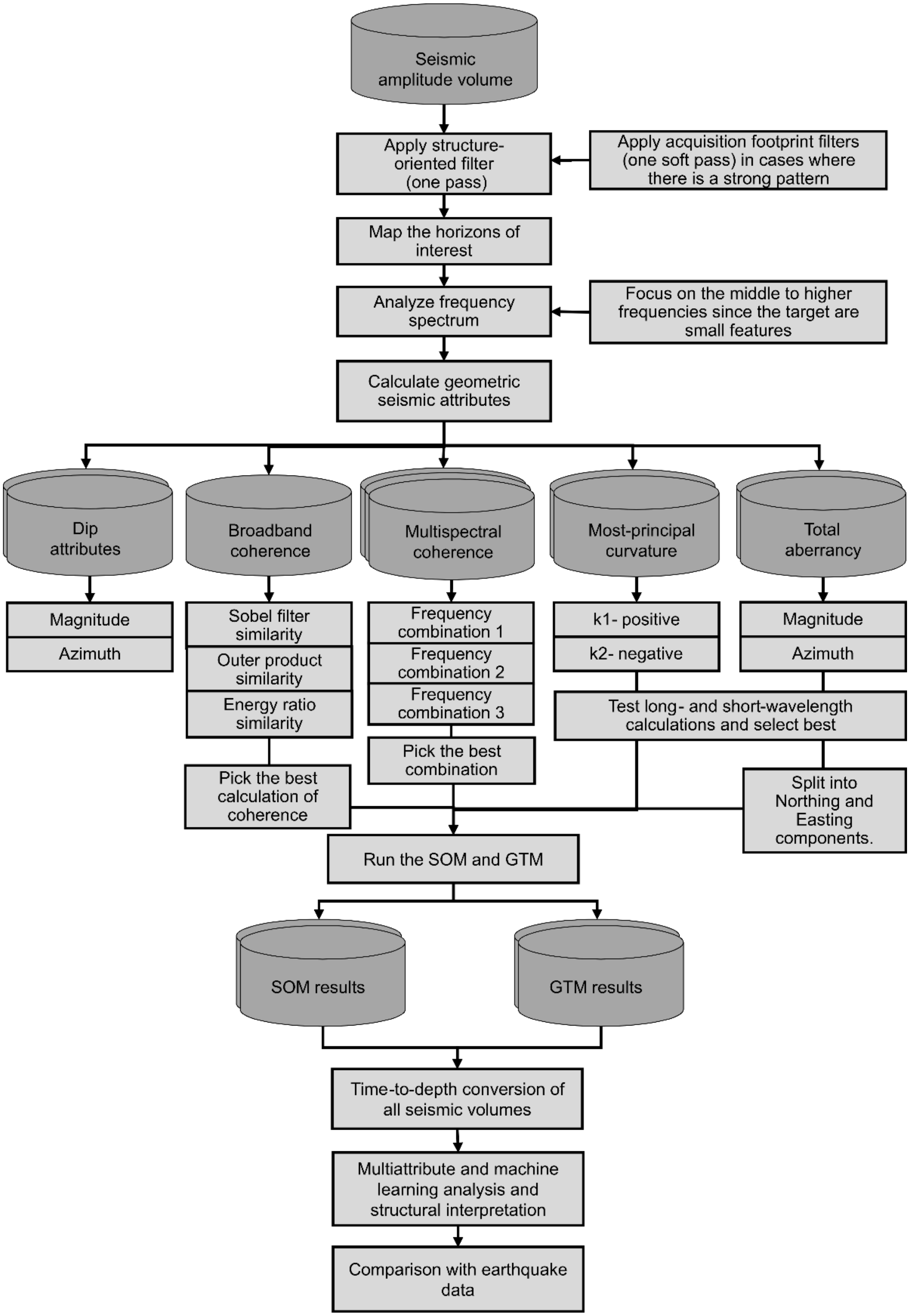

Figure 2-3. Workflow followed.

Fault Interpretation Strategy

There are two seismic imaging challenges in the study area. First, the faults expected are of strike-slip type (Qin et al. 2019). Strike-slip faults have two characteristics that make their mapping in seismic data difficult: their near vertical fault plane and the lack of significant vertical offset large enough to be seen with a limited vertical seismic resolution. And second, the strike-slip faults in the area are basement-rooted faults, therefore, cut mainly the basement interval that corresponds to chaotic seismic facies.

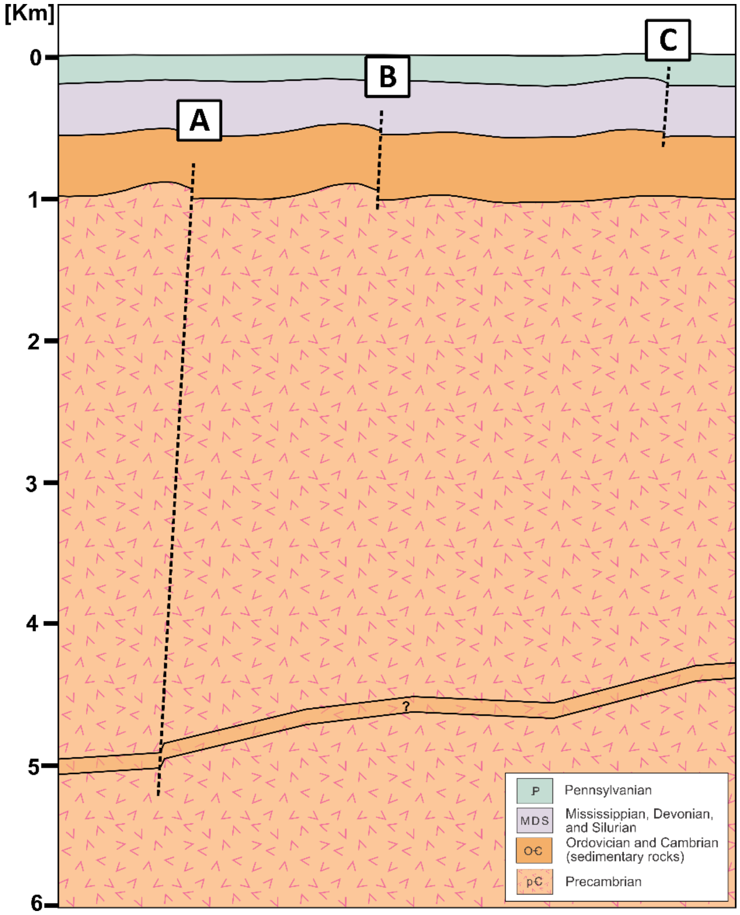

Figure 2-4. Fault interpretation styles. A and B are considered basement-rooted fault as they involve deformation of the basement top, and C are considered faults restricted to the sedimentary section. Schematic representation of faults in the area; depths and thickness not to scale.

For these reasons, our interpretation approach was based on the assumption that lineaments seen at different depths, with different horizons, and different seismic attributes and ML methods, could be inferred to be related to structural features rather than stratigraphic features. In that sense, we picked three horizons at different depths intervals, the top of the Arbuckle Formation (AR), the top of the basement (BR), and the intrabasement reflector (IBR).

During the multiattribute and ML analysis, we analyzed surface extractions over the different horizons trying to identify lineaments potentially associated to discontinuities and that could extend from one depth interval to the other. We compared that with the seismic expression in the vertical section, and further classified the interpreted fault into one of the categories listed in Table 2-1 and shown in Figure 2-4, as well as determined their associated dip and strike. A and B- faults are considered as basement-rooted faults and were the focus of our attention in this study.

Table 2-1. Fault interpretation and classification strategy.

Fault Type	Characteristic
A-faults	Potential discontinuity-related lineaments in the BR and IBR and could be even extended to the AR (Figure 2-4A).
B-faults	Potential discontinuity-related lineament in the BR and AR (Figure 2-4B).
C-faults	Potential discontinuity-related lineaments between AR and an upper reflector, that would indicate they would be restricted to the sedimentary section only, without the influence of the basement (Figure 2-4C).

Seismic Attributes

In this study, we focused only on geometric seismic attributes as the goal was to visualize structural features. Here, we evaluated broadband coherence, multispectral coherence, curvature, and aberrancy. However, dip attributes were also calculated as they are needed for the calculation of any of the other ones considered.

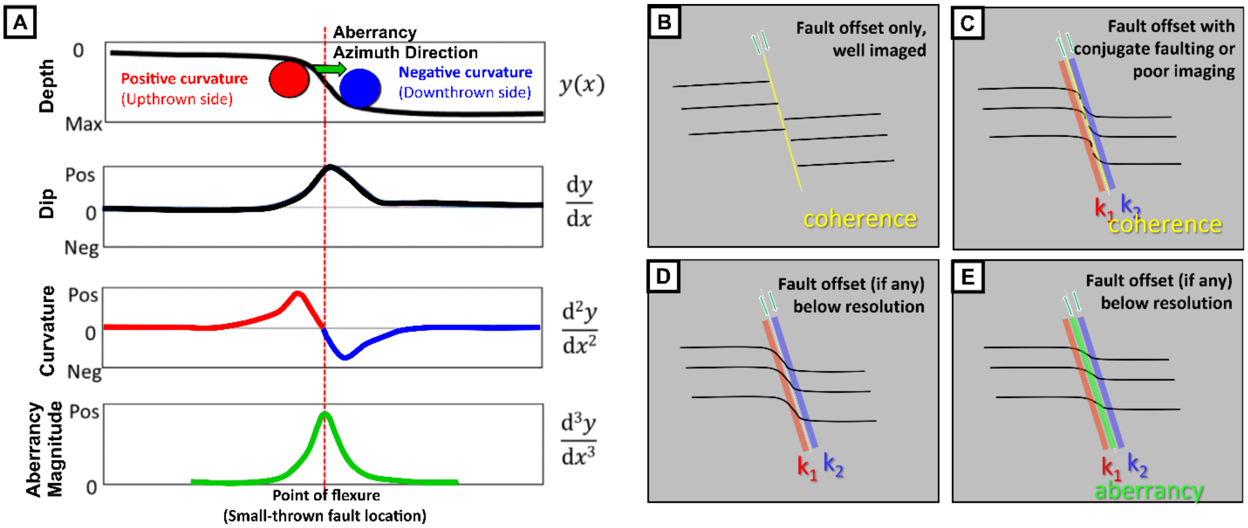

Figure 2-5. A) Mathematical concept behind main geometric seismic attributes (modified from Bhattacharya and Verma, 2019). B) Relationship between the different seismic fault expressions and the geometric seismic attributes of interest (modified from Patel et al. 2021)

Dip Attributes

The relationship between volumetric dip, curvature, and aberrancy is explained in Figure 2-5A and 5B taken from Bhattacharya and Verma (2019) and Patel et al. (2021), respectively. In mathematical terms, dip is the measurement of slopes of the structure (first derivative of the structure), curvature is the measure of the changes in the slope (second derivative of the structure), and aberrancy is the measure of changes in curvature (third derivative of the structure).

A vector dip is used to map the dip and strike of the reflector and is defined by an azimuth and a magnitude (Marfurt, 2006). In that sense, the dip attributes calculations will also have the azimuth and magnitude components that can be display together through co-rendering techniques.

Dip attributes will not be included in the input attribute list for any of the two ML methods, however, as explained by Marfurt (2006), accurate estimation of the vector dip is fundamental for further calculations of geometric attributes, such as coherence, and curvature, as this provides results with higher lateral resolutions and is less sensitive to structural folding.

Coherence

Coherence is one of the most common and well-known seismic attributes for any approach that implies mapping reflector discontinuities in seismic data or analyzing signal-to-noise ratio during processing or filtering steps. Despite the existence of different calculation approaches such as energy ratio, Sobel filter, and outer product, the concept behind continues to be the same: coherence measure the similarity of neighboring traces in the inline and crossline direction, within an analysis window, and considering the structure dip component (Bahorich and Farmer, 1995; Marfurt et al. 1998). However, the main limitation of coherence, or in general any discontinuity-based seismic attribute, is faults with offset below seismic resolution (Gao et al., 2013; Gao and Di, 2015). In these cases, sub-seismic faults may appear as folds adjacent to faults that would be better detected by curvature attributes (Chopra and Marfurt, 2011). Another more recent approach is to apply multispectral coherence.

To be able to capture any potential faults seen as a discontinuity, we tested three different coherence algorithms: energy ratio, outer product, and Sobel filter similarity. However, we decided to further interpret using Sobel filter similarity, since it showed the best signal to noise ratio.

Multispectral coherence

Multispectral coherence is based on the concept that different spectral bands highlight different geological features. In this case, the coherence attribute is calculated from different spectral voice components rather than the full-bandwidth amplitude volume. The volumes are then co-rendered over a RGB (red-green-blue) mixer or added together by combining the covariance matrices of each spectral component (Li et al. 2018). The most important aspect of multispectral coherence is that it is able to show features that may have been lost within the broadband seismic (Chopra and Marfurt, 2018; Li et al. 2018, Lyu et al. 2020).

For multispectral coherence, it was necessary to first make a frequency spectrum analysis and since the target was small scale features, inferred to be lost in the frequency content, we focused on the middle to higher frequencies. Sobel filter similarity was also considered for the calculation of these attributes, and the different combination of spectral voices was done using the RGB blending option.

Curvature

Curvature is another widely used attribute both for structural and stratigraphic seismic interpretation. In structural interpretation its main advantage is that can map subtle sub-seismic faults that lack a clear reflector discontinuity and are rather seen as a fold of the reflector (Chopra and Marfurt, 2011; Figure 2-5C). Chopra and Marfurt (2007) explained in detail the different types of curvatures that can be calculated. In this study, we focused on the most-principal curvature.

Al-Dossary and Marfurt (2006) introduced the multispectral estimates of curvature (i.e long- vs. short-wavelength curvature) which takes into account that geological features can exhibit different curvatures of different wavelengths. According to Chopra and Marfurt (2007) and Chopra and Marfurt (2011), short-wavelengths correspond to intense, but highly localized fracture systems, and longer-wavelengths to a wider and even distribution of fractures. Here, we calculated and tested both options, however, we chose to continue our analysis with the long-wavelength calculations.

Aberrancy

Aberrancy, as presented by Gao et al. (2013), is an extension of the existent curvature attribute. Mathematically, it is calculated as the spatial gradient of curvature, also referred to as flexure. The geological importance of aberrancy is that it is able to map faults with throw below seismic resolution, which means the fault seismic expression is a reflector bend rather than a proper discontinuity (Figure 2-5A and 5E, Gao and Di, 2015). In that sense, it would help map faults that cannot be highlighted with discontinuity-based attributes, such as the conventional coherence attribute.

Gao et al. (2013) introduced aberrancy calculated over a horizon, while Qi and Marfurt (2018) extend it over volumetric calculations. As explained by Qi and Marfurt (2018), 3D aberrancy is defined as a vector with a magnitude, intensity of deformation, and an azimuth, direction in which the curvature decreases in signed value. In this study, we will present these components of the seismic attribute as a co-render of total aberrancy magnitude and total aberrancy azimuth using the long-wavelength estimation.

For the ML step, aberrancy attributes were as well transformed before their inclusion in the attribute list. We separated the total aberrancy vector into its northing and easting components using the following equations:

$$Total\ aberrancy\ magnitude\ \times \sin(total\ aberrancy\ azimuth)$$

$$Total\ aberrancy\ magnitude \times \cos\ (total\ aberrancy\ azimuth)$$

Unsupervised Machine Learning Methods

There are different types of ML techniques that can be applied for fault identification in seismic data, from supervised techniques such as convolutional neural networks (CNN, Wu et al.

2018, Wu et al. 2019, Qi et al. 2020) and probabilistic neural networks (PNN, Mora et al. 2021), to unsupervised techniques such as self-organizing maps (SOM, Hussein et al. 2020; Perico et al. 2021; Qi et al. 2022).

Because of the chaotic seismic facies associated with the igneous basement and the expected strike slip faults in the area, fault mapping with conventional strategies, such as fault stick picking in the amplitude volume, is not possible. Applying PNN would not be the best option because there may not be clear fault planes to pick or track to constrain the seismic attribute responses, especially in the basement interval; and CNN approaches would imply getting rid of seismic attributes and depend solely on training datasets of faulted amplitude volumes in which most of the cases the fault planes are obvious, which is not our case. For these reasons, we focused on SOM and GTM, which allow to integrate several seismic attributes and focus on their combined response to different fault styles.

Self-organizing maps (SOM)

SOM was introduced by Kohonen (1982) and is considered a projection technique that helps representing multidimensional data into a lower dimensional space that further allows to cluster features of similar nature by assigning a 2D color scale. A user-friendly explanation of the mathematical approach behind the SOM method and its application for 3D seismic facies classification was covered by Roy et al. (2011).

Similar to the principal component analysis (PCA) method, SOM starts by plotting the normalized N- input seismic attributes into an N-dimensional space in which the eigenvectors are computed (Figure 2-6A). The eigenvectors are organized by their corresponding eigenvalue, which determines the variance of the data. In that sense, the first two eigenvectors, now called principal components, represent the most important characteristics of the data while the last ones represent uncorrelated noise (Guo et al., 2009). The first two principal components will define the direction of the new 2D latent space that will be further populated with equally spaced prototype vectors, which will also define the initial number of classes/clusters (Figure 2-6B).

A common practice is to over-define the number of prototype vectors and allow the method to find convergence into a lesser number of clusters (Roy et al., 2011). In our specific geoscience case, we are limited by the number of colors that can represent each cluster, being 256 the most common available amount in different software packages. In that sense, we start by defining 256 prototype vectors.

During the training process, these prototype vectors will move, therefore deforming the 2D projecting space, now called manifold, to better fit the input data vectors (Figure 2-6C). This process will iterate several times, moving prototype vectors in each iteration, until it finds a convergence. At the end, the initial protype vectors will have grouped themselves into a lower number of separate clusters that represent the input data and that can be visualized by using a 2D color scale (Figure 2-6D; Roy et al., 2011).

The final clustering process of the 3D volume is done by assigning to each voxel in the seismic data the color associated to the prototype vector that is closest to the data vector representing that specific voxel. In that sense, voxels in the seismic volume with similar colors indicate similar nature, while voxels of different color indicate different nature (Roy et al., 2011).

Nevertheless, SOM has several limitations, during the training process and the final clustering, with parameters such as training radius, neighborhood function, and learning rate; or steps such as the definition of a cost function to indicate convergence of iterations and, the most significant, the lack of probability density functions as measure of confidence in the clustering results (Roy et al. 2014; Zhao et al., 2015; and Chopra and Marfurt, 2018c). To improve and solve most of these limitations, Bishop et al. (1998) introduced the GTM method as a more probabilistic reformulation of the widely applied SOM.

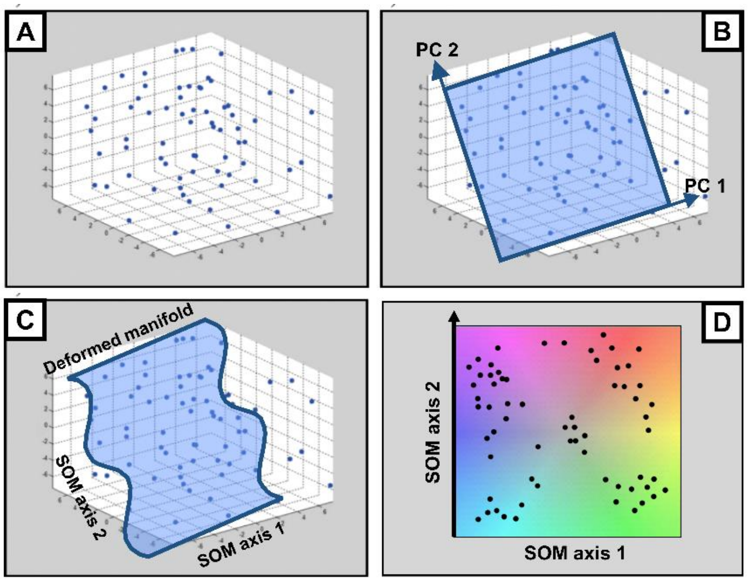

Figure 2-6. Simplified projection steps in SOM, A) data are plotted in a multidimensional space, B) eigenvectors are computed and the principal components (PC) are determined to further select the initial manifold and start populating it with prototype vectors, C) manifold deforms to fit the natural clusters, D) prototype vectors are mapped against a 2D color bar (modified from Zhao et al. 2015b).

Generative topographic mapping (GTM)

Bishop et al. (1998) indicates that GTM is a non-linear dimension reduction technique that makes use of latent variable models to allow non-linear transformations to find correlations or patterns between data points. This method is based on Gaussian mixture models that are optimized using the expectation-maximization (EM) algorithm.

As explained by Bishop et al. (1998) and Roy et al. (2014), in contrast to other models used for visualization, where the projection is done from the N-dimensional space to the 2D visualization space, GTM model is defined by mapping regularly spaced grid points (**u** in Figure 7A) from the 2D latent space into the N-dimensional data space by using non-linear basis functions (**j** in Figure 2-7A). In the N-dimensional data space, the initial latent space grid points are now represented by vectors (**m**) that form a 2D non-Euclidian manifold (Figure 2-7B).

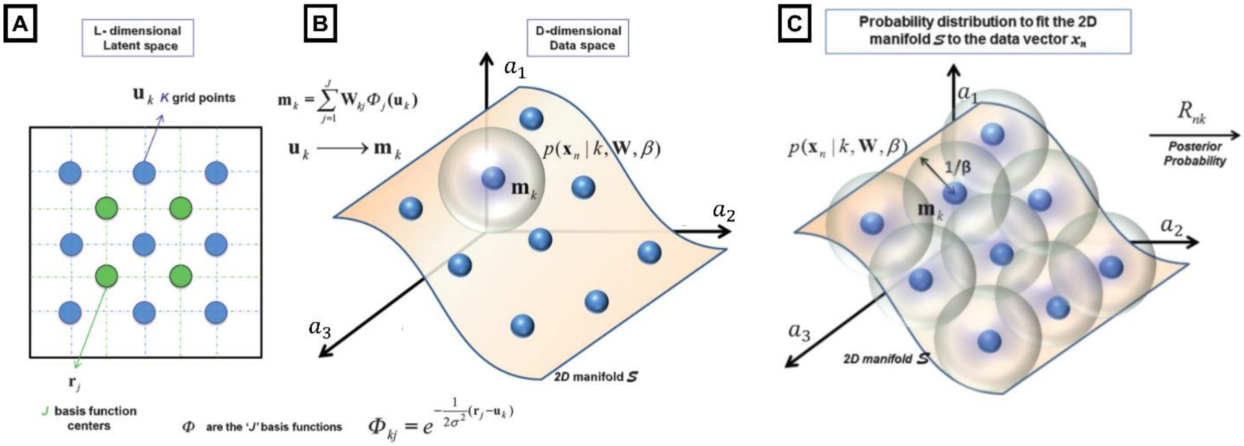

Figure 2-7. Simplified steps in the GTM method. A) regularly spaced grid points in the 2D latent space, B) 2D non-Euclidian manifold in the N- dimensional data space, and C) probability functions centered on the **m** vector (modified Roy et al. 2011 and Zhao et al. 2015b).

Each **m** vector inside the manifold will be assigned a probability function of representing a data vector **x**, and a Gaussian mixture will be formed by integrating these probability functions (Figure 2-7C). In other words, by using Gaussian probability density functions centered on the reference vectors, GTM indicates the vector that is most likely to be associated with a data point, but also the probability of that specific data point belonging to one vector or another (Zhao et al., 2015b).

In the training process, and through iteration and application of the EM algorithm, the probability density functions will accommodate to better represent the data vectors until convergence. Finally, and using Bayes' theorem, the final posteriori probabilities of the data vectors are calculated and projected back to the 2D latent space where clustering can be made (Roy et al., 2014).

In this way, by using Gaussian mixtures model and EM-algorithm, GTM solves many of the issues associated to the SOM method, such as the mentioned lack of theorical basis for choosing training parameters and proof of convergence, and the lack of a measure of confidence in the clustering process.

Velocity Model and Depth Conversion

For the velocity model we used different data and parameter constraints from the literature. We used a 1D local S-wave velocity model and a Vp/Vs ratio equal to 1.73 from Tan et al. (2020) to calculate the P-wave velocity. We estimated the expected basement top depth to be between 0.914 and 1.07 km (true vertical depth sub-sea, SSTVD), from the elevation map of the Oklahoma basement presented by Crain and Chan (2018), as well as the closest basement-penetrating wells from Campbell and Weber (2006), which indicate basement depths ~1 km (SSTVD).

We created a two-layer 3D velocity model, the first layer corresponding to the sedimentary section and first meters of the basement, and the second layer assuming the intact basement. We used an average velocity of 3.5 km/s for the first layer of 1.5 km, and we left the same calculated P velocities for the rest of the section (Appendix. Table 1). The 1D P-velocity model estimated from Tan et al. (2020) is shown in Figure 2-8B and the 3D velocity model derived from it is shown in Figure 2-8C. The converted seismic data to depth is shown in Figure 2-9.

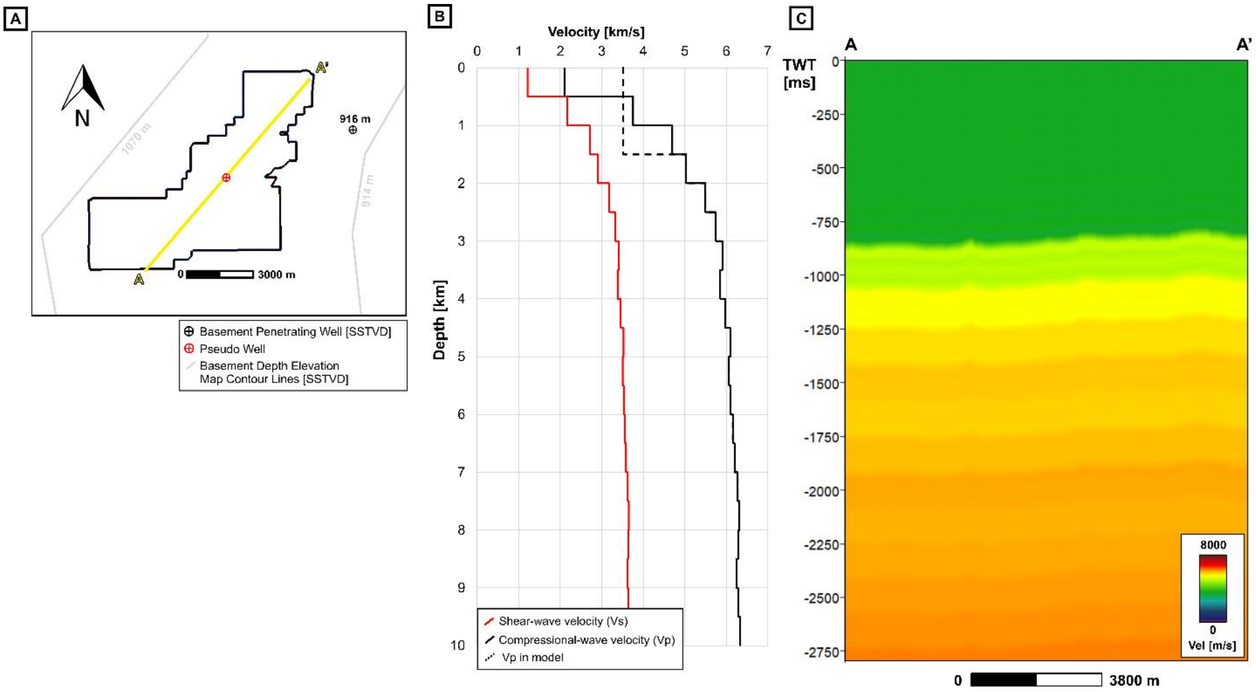

Figure 2-8. A) Location of the closest basement-penetrating well and contour lines of the elevation map of the Oklahoma basement (from Campbell and Weber, 2006 and Crain and Chan, 2018), B) 1D P-velocity model estimated from the S-velocities presented in Tan et al. (2020) and C) derived 3D velocity model.

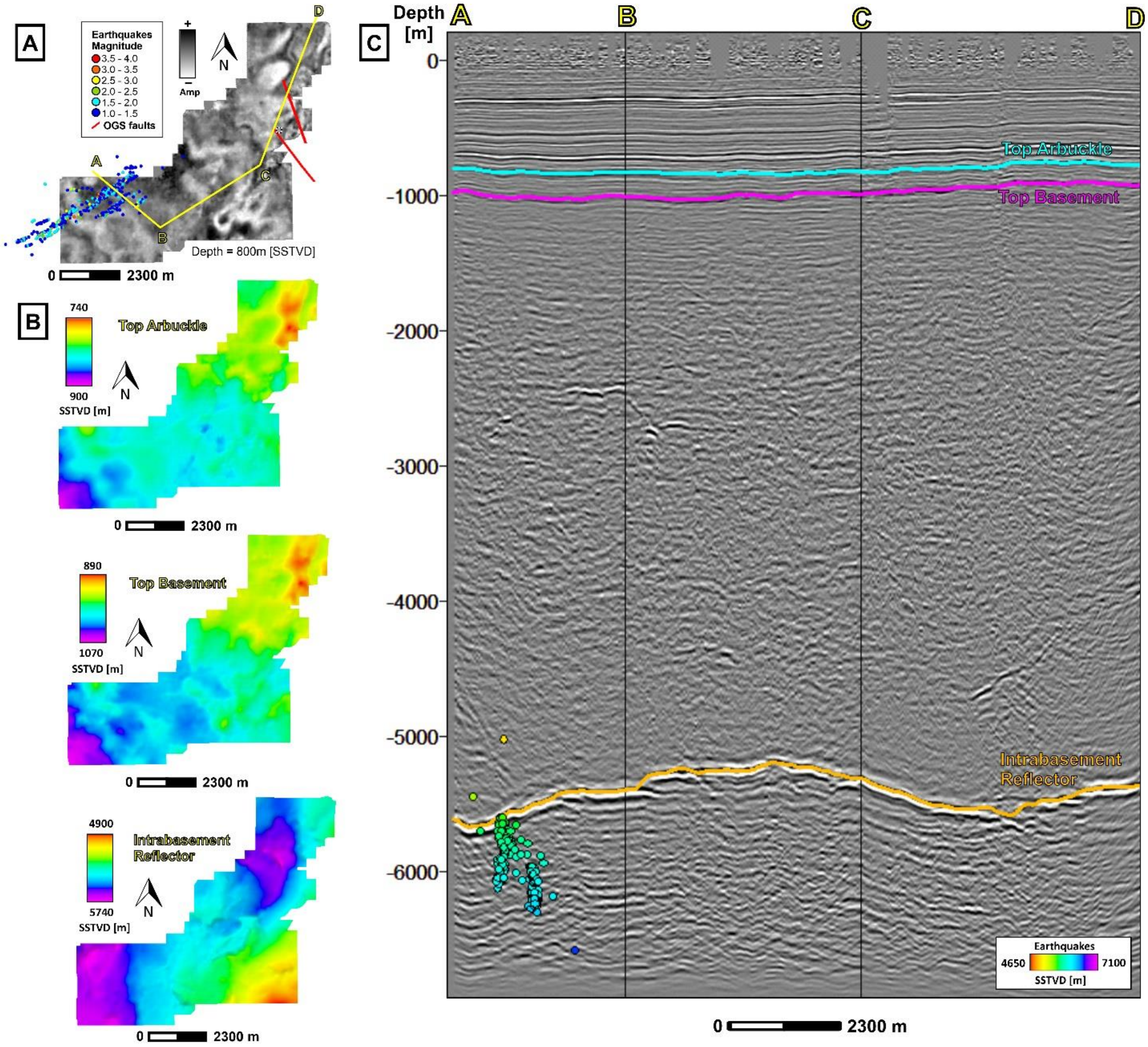

Figure 2-9. A) Depth slice at 800 mSSTVD with the earthquake data projected to the horizontal plane, B) top of the Arbuckle, top of the basement, and intrabasement reflector horizons after time-to-depth conversion, C) ABCD cross section covering the NE, central, and SW areas of the seismic volume converted to depth, earthquake data projected to the cross-section for reference.

RESULTS

Multiattribute Analysis

The results of the multiattribute analysis are shown in Figure 2-10 for the three horizons of interest: top of the Arbuckle, top of the basement, and the intrabasement reflector.

Figure 2-10A shows the surface extractions of the broadband coherence results. Notice that we can see some discontinuities marked by the red arrows on all three horizons; we have labeled them as sharp lineaments. At the top of the Arbuckle there are three lineaments (L1, L2, and L3) seen with NE-SW strikes. At the top of the basement, only L1 can be inferred and a potential fourth lineament, L4, in the noisier area to the NE can be seen. The discontinuities in the IBR are very well visualized and many lineaments are detected. Notice we can see some discontinuities that could be correlated with the continuation of L1 and L2 in depth. Another lineament, L5, is seen between L1 and L2, also showing a NW-SE strike. To the NE of the volume, we can see several discontinuous patterns, and we can infer a possible lineament that could correlate with L4 of the upper horizons.

Figure 2-10B shows the RGB (red-green-blue) blend of the spectral calculations of coherence at 38 Hz, 49 Hz, and 60 Hz, and the surface extractions for each horizon of interest. Similar observations to those seen with broadband coherence can be made, however, observe that at the top of the basement lineament L1 is more clearly seen and L2 starts to appear. In the IBR, the discontinuities are better highlighted as well and the possible continuations of L1, L2, L4, and L5, in depth can be inferred.

Both broadband and multispectral coherence over the IBR horizon show many more other lineaments than the upper horizons, some of them with an almost N-S strike besides the predominant NE-SW direction. However, we have labeled and focused only on those that can be correlated with the shallowest lineaments as this would provide more confidence on the mapping of potential basement-rooted faults in the sedimentary section. More intense deformation or fracturing of the basement evidenced by these discontinuities over the inferred mafic intrusion should not be discarded.

The co-render of long-wavelength k1-most positive and k2-most negative curvature are presented in Figure 2-10C. Here, the linear patterns change drastically as we cannot longer see sharp lineaments, but rather broad lineaments (yellow arrows) marked by positive and negative curvature anomalies. This attribute better highlights features most likely related to folds in the reflector, more specifically, the positive curvatures would indicate anticlinorium-shapes, while negative curvature would indicate synclinal-shapes. Notice there are some clear positive anomalies that show a linear and a parallel-to-each-other pattern. To the NE of the seismic volume, both in the top of the Arbuckle and the top of the basement, we can see positive curvatures labeled as L4, L6, and L7, and that have a NE-SW direction. To the SE, we can see two positive anomalies as well, labeled as L1 and L8, and that has a NE-SW strike. And to the SW, we can see two other positive anomalies, L9 and L10, with an almost E-W strike, and a negative anomaly with a NE-SW strike, L11. Two smaller features can be seen in the center, L2 and L3. In the IBR, we can only see one clear negative feature that we could correlate with the projection in depth of a potential fault L1.

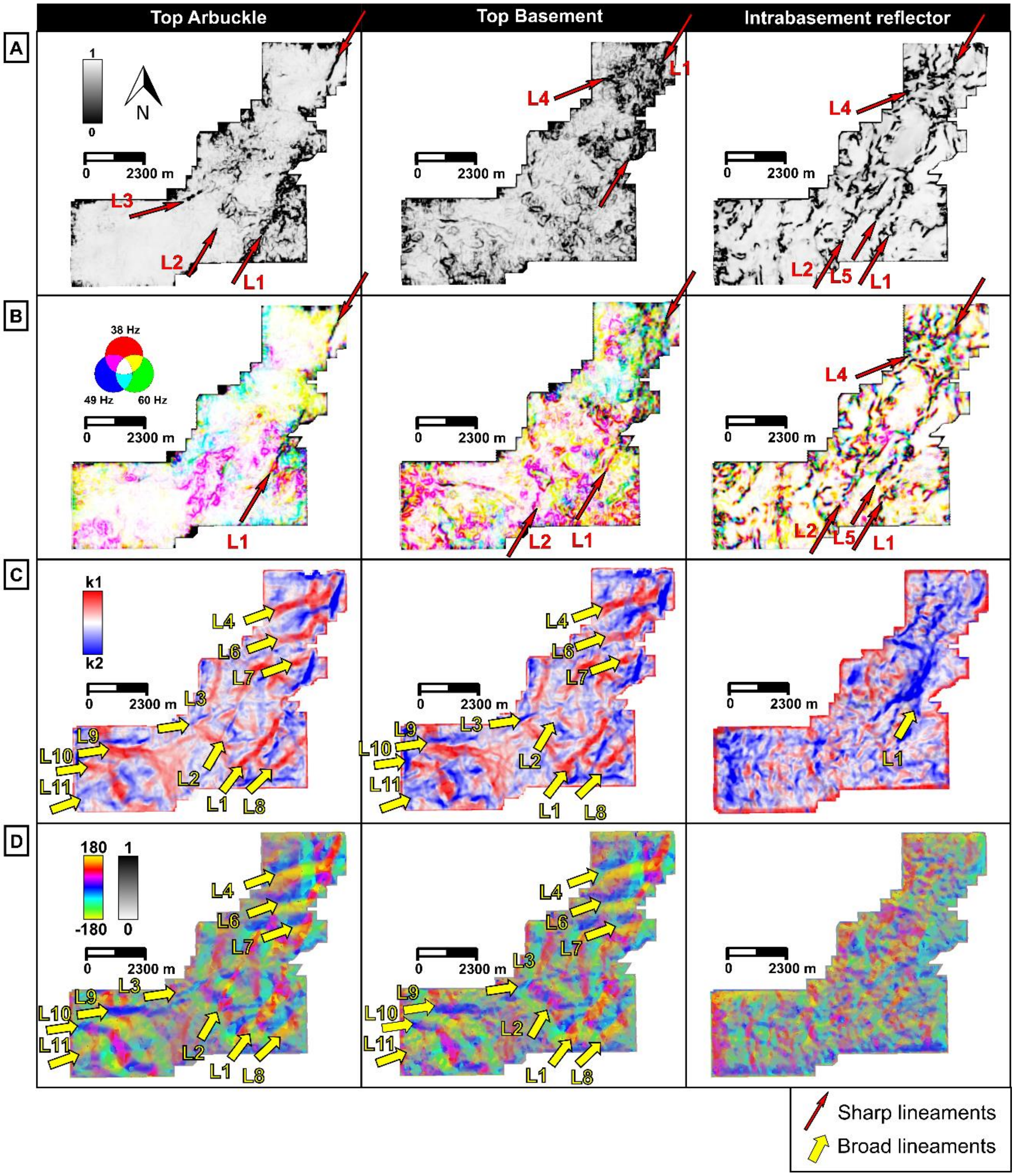

Figure 2-10. Multiattribute analysis results, A) broadband coherence, B) RGB blend of the multispectral coherence combination of 38 – 49 – 60 Hz, C) co-render of long-wavelength most-positive curvature k1 and most-negative curvature k2, D) co-render of long-wavelength total aberrancy magnitude and total aberrancy azimuth.

Figure 2-10D shows the co-render of long-wavelength aberrancy magnitude and aberrancy azimuth. In the aberrancy attributes, we can see now the flexures associated with the previously identified curved features. Notice that the previous positive anomalies labeled as L4, L6, and L7 can be seen in the top Arbuckle and top basement with the aberrancy attributes as a double signature flexure, dark blue and yellow, which can be correlated to each side of the positive anomaly, when it changes from negative to positive and positive to negative again. The same double flexure signature can be seen for L8, L9, and L10. However, what we labeled as L1 and L2 in the aberrancy extractions for the top of the Arbuckle and top of the basement have mainly a single flexure pattern in red for both lineaments, while the L11 show a much broader single flexure in yellow towards. In the IBR not much information can be extracted.

Unsupervised Machine Learning

The integration of all geometric seismic attributes using SOM and GTM methods and the surface extractions over each ML volume are shown in Figure 2-11A and 11B, respectively. Notice that both SOM and GTM show similar images, however, the surfaces extractions over the GTM volumes show clearer patterns and the contrast between clusters is better highlighted than those obtained with the SOM. In any case, when integrating all data in a single volume using ML it is easier to correlate the relationship between the sharp and broad lineaments seen during the multiattribute analysis and at different depths.

Notice that both in the SOM and GTM, there are some orange to pink clusters, in the top Arbuckle and top basement, that align with the location of broad lineaments associated with positive curvature anomalies seen during the multiattribute analysis stage. This would indicate areas of potential folding with anticlinorium shapes. This is true for the lineaments labeled as L4, L6, L7, and L8, but also for the areas close to sharp lineaments labeled as L5, L9, and L10.

Notice that with the ML surface extractions, more information can be inferred regarding the sharp features. In the previous multiattribute step we labeled L9, L10, and L11 as broad lineaments, however, notice they look sharper in the ML. In fact, lineament L11 is much clearer than in the multiattribute analysis, in the ML extractions it can be inferred due to its very linear and sharp break from the orange/pink clusters to those greener to yellowish. The same happens for lineaments L2 and L3, both in the top Arbuckle and top basement, which are seen as sharp features.

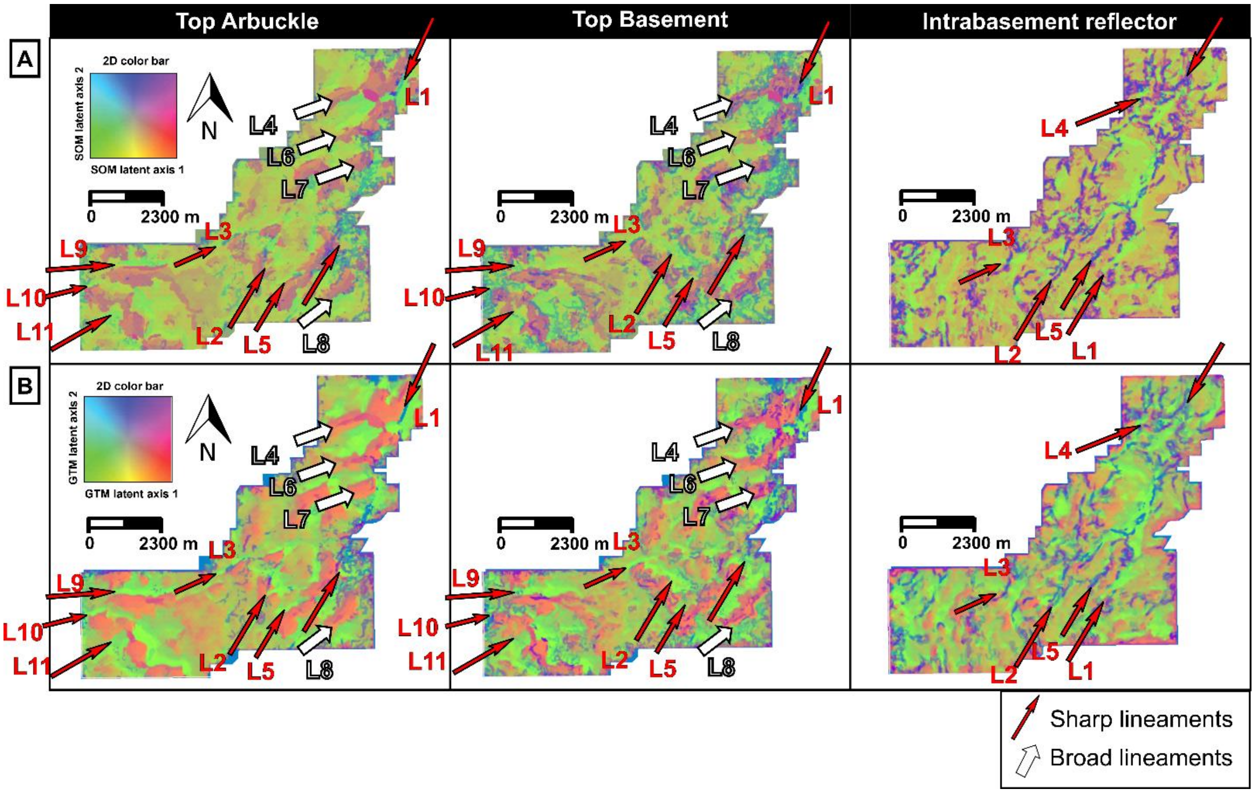

Figure 2-11. Machine learning results and surface extractions over the horizons of interest. A) SOM results and B) GTM results.

Lineament L1, though, has a different expression, and it is associated with blue and purple clusters in the top Arbuckle and top basement. These clusters seem to be associated with areas where we saw clear discontinuities marked by the broadband and multispectral coherence. Notice the same can be observed in the IBR. Purple to blue clusters show the areas of sharp discontinuities and that could be associated to the projection in depth of the lineaments L1, L2, L4, L5, and potentially, L3.

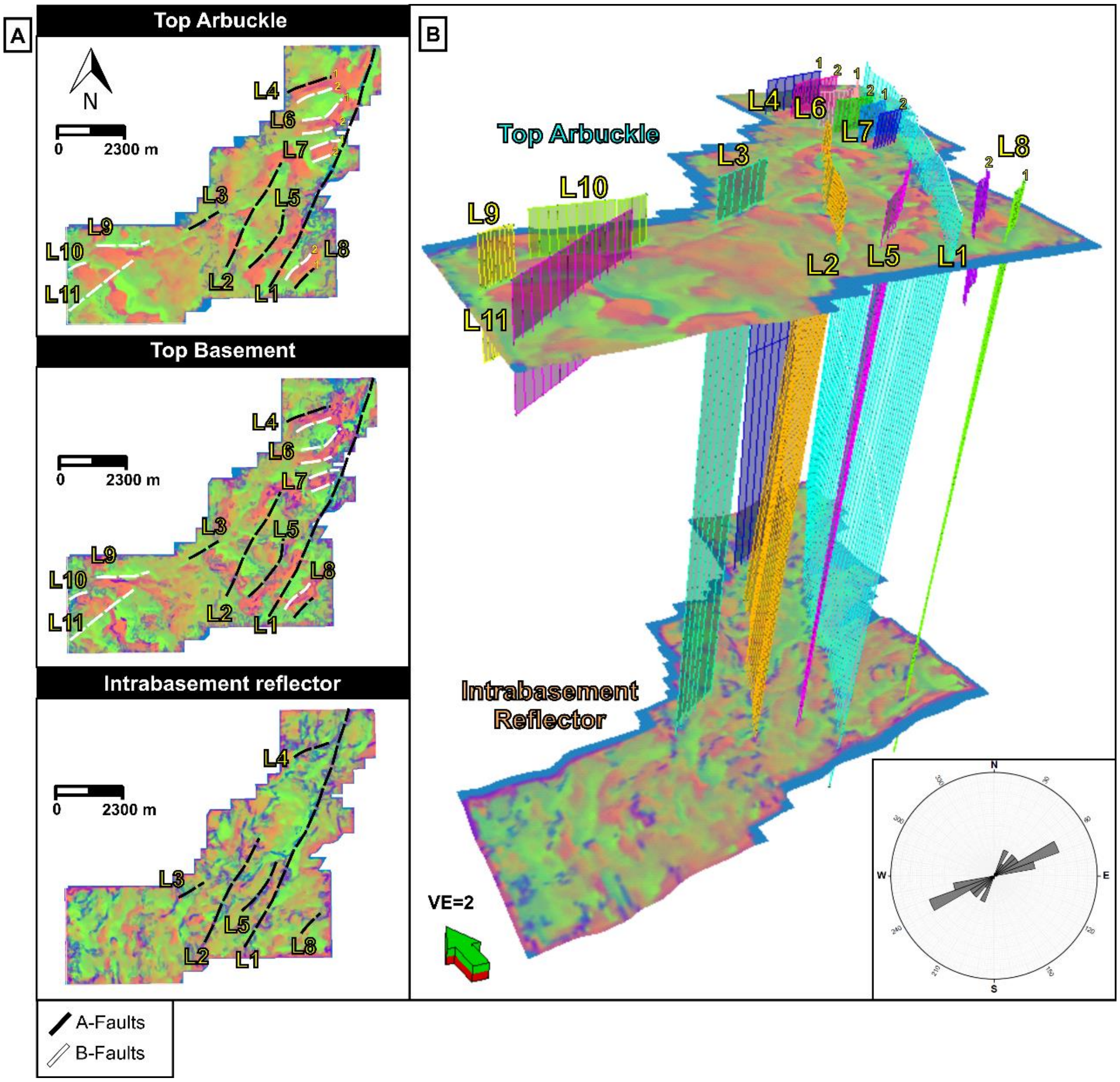

Figure 2-12. Interpretation of potential basement-rooted faults using the GTM results. A) 2D view, per horizon of interest, and B) 3D view correlating IBR and AR. Inset image shows a rose diagram with the strikes calculated for the faults interpreted with the seismic derived outputs.

Basement-Rooted Fault Interpretation

Figure 2-12 shows the interpretation of potential basement-rooted faults both in 2D view, per horizon of interest, and 3D view, along with a rose diagram of the strikes calculated. Notice in Figure 2-12A, we have colored coded the interpreted faults as A or B- fault type (black and white, respectively) following the fault interpretation strategy previously shown in Figure 2-4 and Table 2-1. The details of each fault interpreted are presented in Table 2-2, and several cross sections are shown in Figure 2-13 and 2-14. These cross sections were used to 1) guide the structural interpretation along the different depth intervals, 2) classified the potential faults depending on their integrated seismic expression (using the inputs obtained from the seismic attributes, machine learning, and amplitude volume), and 3) calculated dips and strikes.

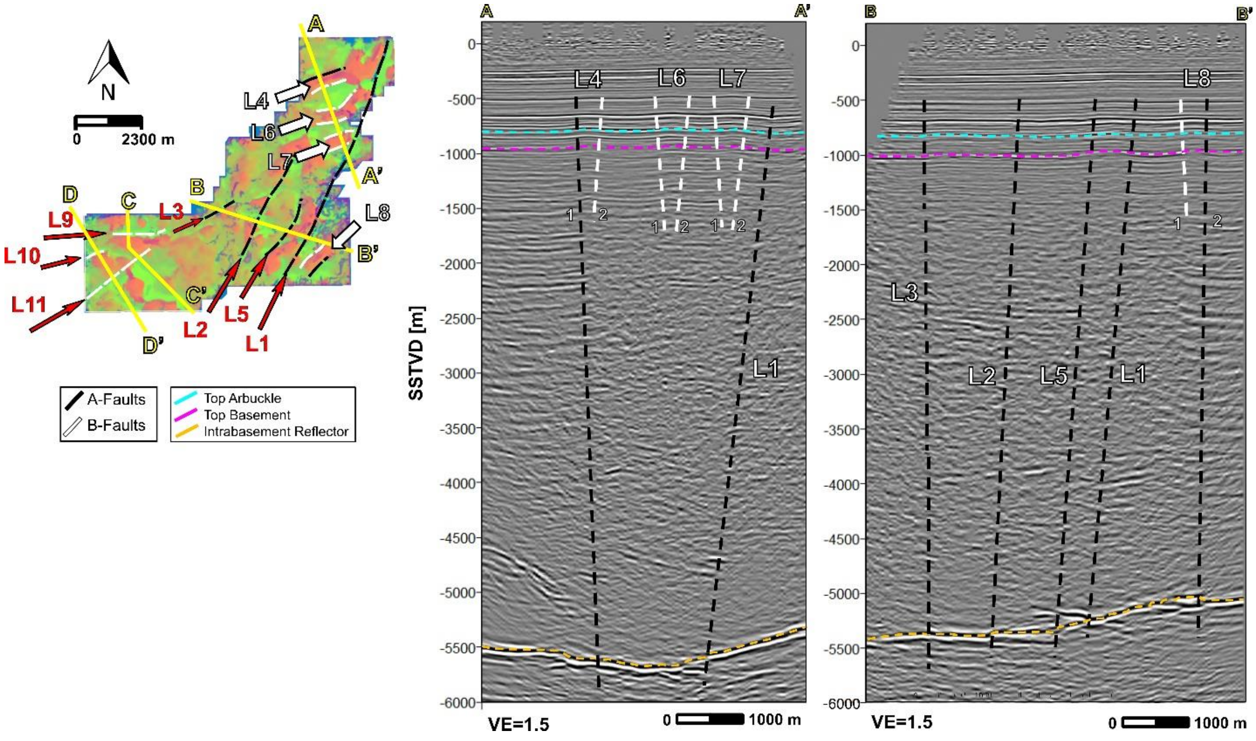

Figure 2-13. Cross sections A-A' and B-B' covering the northeastern and central areas of the seismic volume.

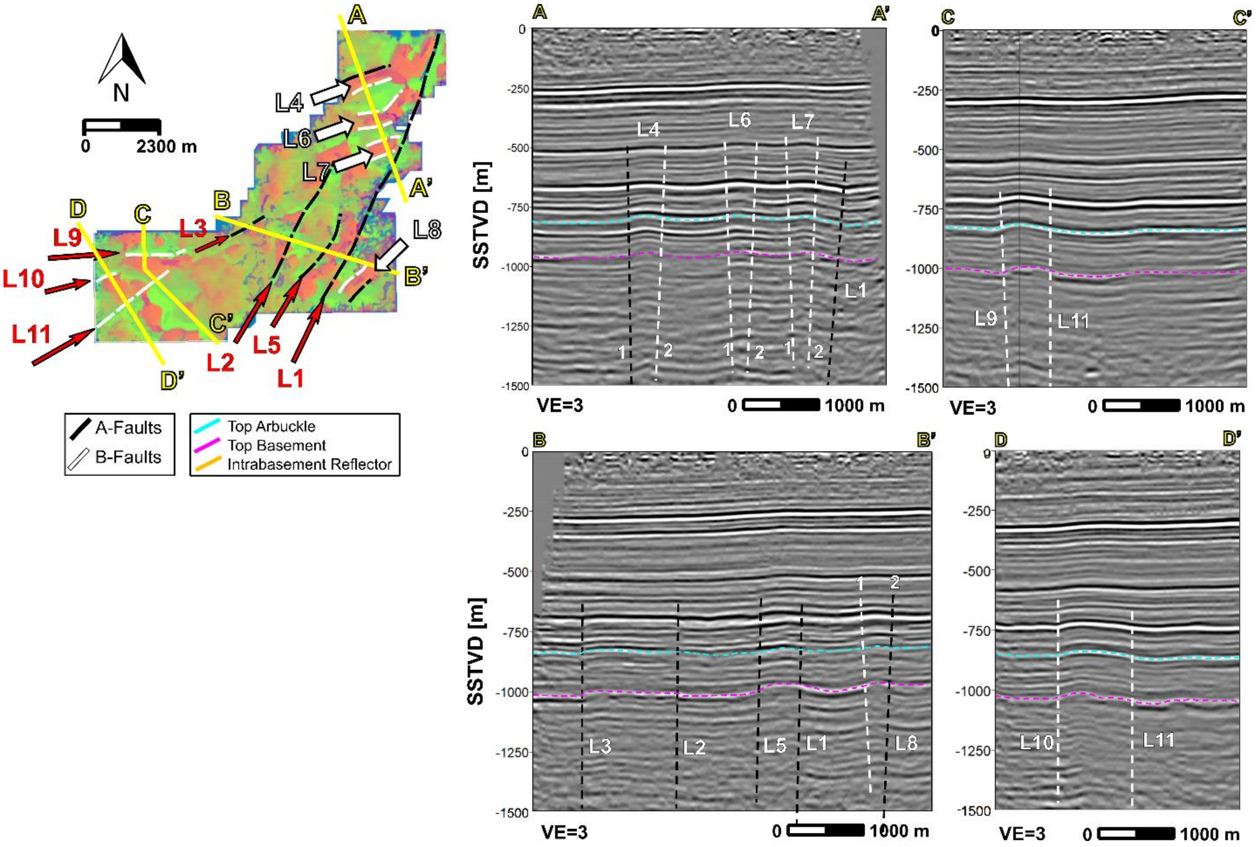

Figure 2-14. Cross sections focusing on the upper section of the seismic volume from top of the basement to the top of the Arbuckle and the overlying sedimentary strata.

Cross section A-A' focused on the three folded structures in the NE side of the seismic volume (Figure 2-13 and 2-14). Notice that the flexure related to these structures extends from the basement top far up into the sedimentary section overlaying the Arbuckle. The fact that we could see several discontinuities below in the intrabasement reflector could also suggest there is a structural control between the anticlinorium-style folds and pre-existent basement structures. Because of this, we have considered the potential existence of a fault at each side of these folds, and that could be controlled or joined to faults coming from the basement. We have labeled them as L4-1, L4-2, L6-1, L6-2, L7-1, and L7-2. From these potential six faults, L4-1 could be interpreted as an A-type basement-rooted fault, as we could track it in the basement top and correlated it with discontinuities seen in the IBR. The other potential faults, L4-2, L6-1, L6-2, and L7-1, L7-2, could be B-type, which means they could be tracked from basement top into the upper sedimentary section, but could not be tracked in the IBR. The fault interpreted as L1 can also be seen in the cross-section A-A'. Notice its expression is much clearer than the others. In Figure 2-13, we can see discontinuities both in the upper sedimentary section and BR, and the deeper IBR. We have interpreted this potential L1 basement-rooted fault as an A-type.

Cross section B-B' focuses on potential faults mapped in the center and SW area of the seismic volume (Figure 2-13 and 2-14). Notice most of these faults have an A-type expression, as they could be tracked from the top of the Basement to the IBR. The potential faults L1, L2, and L5 seem more intuitive than the others. Notice they show a clear alignment of discontinuities in the IBR, and a series of different fault expressions in the upper section, from small discontinuities, to folded reflectors, and strong flexures, as well as clear lineaments in the ML extractions. These faults are those we mapped with the most confidence than the others seen with an A-type expression. On the other hand, L3 shows a sharp flexure both in the AR and BR as well as clear lineament in the ML extractions, which would indicate B-type expression. However, it could be tracked to the IBR and connected with a shorter alignment of discontinuities. In that sense, we could as well classify it as an A-type with less confidence than a B-type. Similar to L4, L8-1 and L8-2 are potential faults associated with anticlinorium-shape features seen as folded basement and Arbuckle top, and folded overlying strata. L8-2 could be correlated as well with a short alignment of discontinuities in the IBR.

Cross-section C-C' and D-D' focused on the potential faults mapped to the SE side of the seismic volume (Figure 2-14). Potential faults L9 and L10 were seen with sharp flexures, associated folded reflectors, and a clear linear pattern in the ML extraction. In the amplitude section, we can see those patterns very clearly, a subtle break in the basement top and sharp flexures in the upper reflectors and far up from the Arbuckle. In the IBR, there were no discontinuities that could be correlated, and we considered these potential faults as basement-rooted faults with B-type expression. The potential fault L11 is the least intuitive, despite that it was clearly seen with the ML as a sharp change from one type of clusters to the other, its expression was not so clear in the seismic attributes. It was marked as a negative curvature alignment and a very broad flexure. In the amplitude volume it is as well shown as subtle flexure of the reflectors from the basement to the Arbuckle. We classified it as a potential basement-rooted fault with a B-type expression.

Table 2-2. Classification, dip, and strike of potential faults interpreted using multiattribute analysis and ML methods.

Lineament	More confident classification	Less confident classification	Dip [°]	Strike [°]	Vertical Extension	Observation
L1	A		84	205	Above Arbuckle	Discontinuities seen in AR, BR, and IBR, as well as associated folded reflectors and flexures.
L2	A		85	206	Above Arbuckle	Discontinuities, folded reflectors, and sharp flexures in the AR and BR. In the IBR, there is a clear long alignment of discontinuities.
L3	B	A	89	61	Above Arbuckle	Short discontinuities, folded reflectors, and sharp flexures in the AR and BR. In the IBR, it could be connected to a short alignment of discontinuities.
L4_1		A	87	69	Probably above Arbuckle (overlying strata is folded)	Folded reflectors from BR to AR and overlying strata. Discontinuities in the IBR.
L4_2		B	86	249		Folded reflectors from BR to AR and overlying strata. Broad flexures to each side of the positive curvature anomaly. It could possibly connect with major L4_1 fault.
L5	A		86	215	Above Arbuckle	Discontinuities in the IBR, folded reflectors, and flexures from BR to AR and overlying strata.
L6_1		B	82	60	Probably above Arbuckle (overlying strata is folded)	Folded reflectors from BR to AR and overlying strata. Broad flexures to each side of the positive curvature anomaly. They could possibly connect with major faults, L1 and L4_1.
L6_2		B	82	260		
L7_1		B	84	66		
L7_2		B	81	248		

L8_1		A	89	221		Folded reflectors from BR to AR and overlying strata. In the IBR, it could be connected to a short alignment of discontinuities.
L8_2		B	82	44		Folded reflectors from BR to AR and overlying strata. Broad flexures to each side of the positive curvature anomaly. It could possibly connect with major L8_1 fault.
L9	B		85	79	Above Arbuckle	Strong flexure of the BR (subtle discontinuity also seen in cross section), folded AR and upper horizons.
L10	B		88	72	Above Arbuckle	Strong flexure of the BR, folded AR, and upper horizons.
L11		B	89	51	Probably above Arbuckle (overlying strata is flexure)	Subtle flexure on the BR, and upper AR. Sharp break in the ML results.

Comparison with Earthquake Data

Figure 2-15A shows the comparison between the basement faults lineaments marked by earthquake data (from the catalog of Park et al. 2022) and the faults interpreted in this study using seismic attributes and ML methods. Notice the easternmost fault tip of the potential fault L9 coincides with one of the smaller clusters seen with the earthquake data. A similar situation happens with the potential fault L10, which seems to coincide with some smaller events to the west. More noticeable from all of them is lineament L11 which was seen as a very sharp linear contrast in the ML extractions. L11 coincides with one of the largest clusters seen.

Figure 2-15B and C compare the rose diagram created using the strikes direction of the faults mapped with the seismic data and the rose diagram created using lineaments seen from the visual clustering of earthquake events (Figure 2-15D; Appendix, Figure 1 and Table 2). The potential basement-rooted faults mapped in the area showed strikes ranging from 25°/205° to 80°/260°, and a mean vector of 57°/237°, while earthquake data show strikes ranging between 45°/236° and 90°/260°, and a mean vector of 61°/241°. Finally, the earthquake's depths are between 4650-7100 mSSTVD, which is very deep into the basement and sometimes below the IBR (Figure 2-15E), which is between depths of 4900 and 5740 mSSTVD.

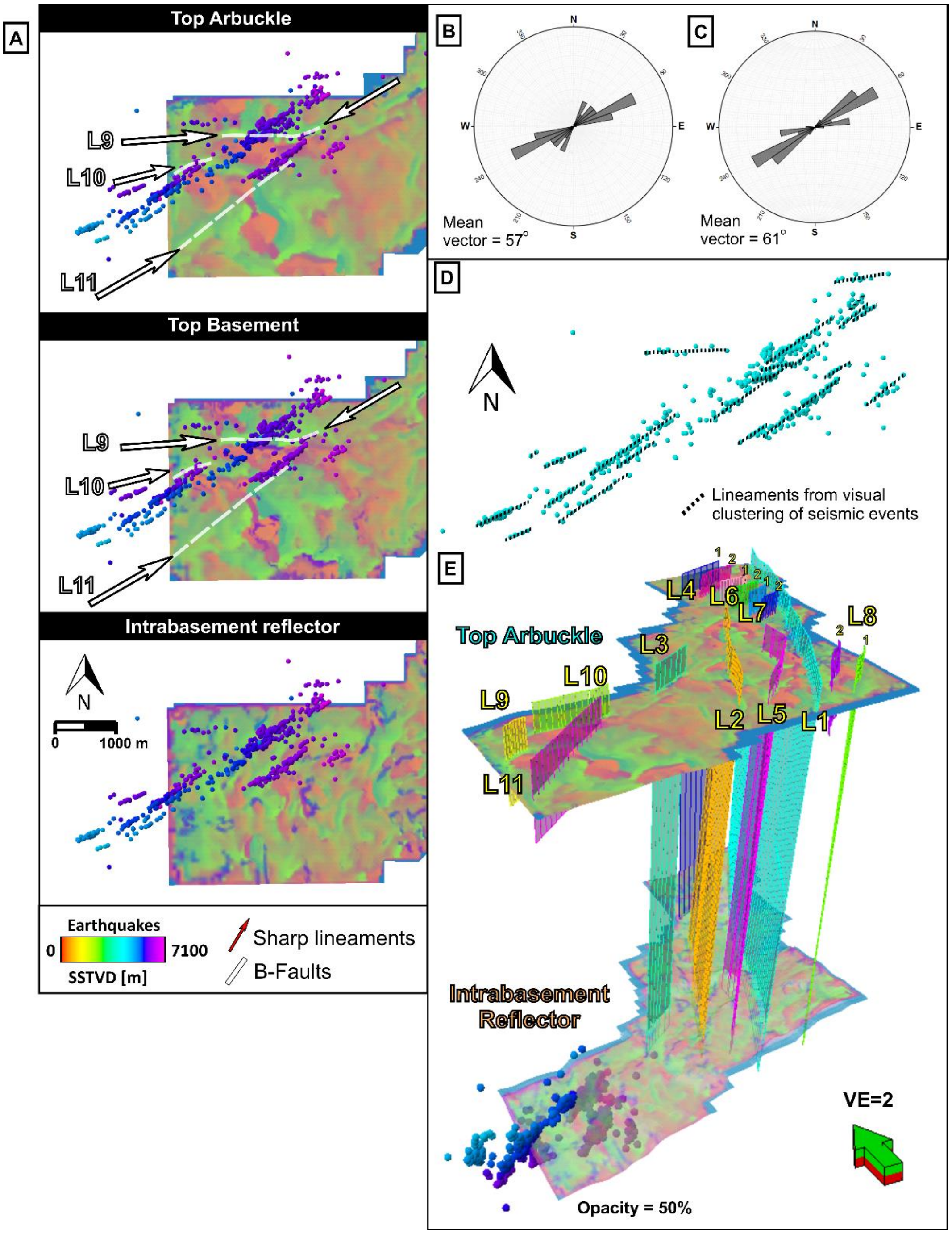

Figure 2-15. A) Comparison between the horizontally projected earthquake data and the faults interpreted using seismic attributes and ML methods, B) and C) rose diagrams comparing faults interpreted in the seismic volumes and lineaments from earthquake data, respectively, D) lineaments interpreted from visual earthquake clustering, and E) 3D view of the seismic events and the interpreted faults.

DISCUSSION

Applicability of Multiattribute Analysis and Machine Learning Methods

The results presented in this study showed how multiattribute analysis and ML methods helped identify potential basement-rooted faults in a dataset in northcentral Oklahoma. Through correlation between different horizons surfaces at different depths, it was possible to identify eleven potential basement-rooted faults of which at least six could be tracked all the way to the IBR. Some of these potential faults were mapped with more confidence than others. L1, L2, and L5 were mapped with a higher level of confidence as they show clear evidence of discontinuity in the IBR and co-located lineaments in the BR and AR, therefore, having an A-type basement-rooted fault expression. On the other hand, L3, L9, and L10 were also mapped with more confidence as a B-type basement-rooted fault expression as they show clear evidence of discontinuity and sharp flexures and lineaments over the BR and AR.

However, ML extractions were critical to identifying potential faults such as L11 that showed more subtle expressions in the multiattribute analysis and were mapped with less confidence. L11, along with L9 and L10, also interpreted with less level of confidence, were mapped near the horizontal projection of much deeper earthquake events and showed similar strikes as well. Despite L11 being mapped with a lower confidence level when compared with other potential basement-rooted faults in the area, it was still more clearly seen with ML extractions. In that sense, the application of ML methods would be an important complementary tool that can help expand or provide other insights, especially for features that could escape from multiattribute analysis.

Regarding the comparison between the two different unsupervised ML methods, SOM and GTM, we could evidence the clear improvement in the clustering when using GTM over SOM.

This can be an expected result as the GTM method was designed as a reformulation of the SOM method that helped solve one of its main drawbacks, the lack of confidence measurement in the clustering step, by using probabilistic density functions that allow the prototype vectors to better fit the data points, therefore, improving the clustering results, and final visualization.

However, something that is noteworthy to mention for both ML methods tested is that they both allowed the integration of the different seismic fault expressions into a single volume which not only facilitated the structural interpretation but also helped highlight potential basement-rooted faults that are most likely to be missed if using only multiattribute analysis.

Correlation with Hypothesis of the Oklahoma Basement Deformation

The results observed in the multiattribute analysis correlate with what previous authors have proposed for Oklahoma (Figure 2-16). Kolawole et al. (2019, 2020) inferred that the basement faults detected through seismic activity correspond to pre-existing basement faults that further propagated into the sedimentary section and were later reactivated through wastewater injection into the Arbuckle. Therefore, it would be expected for these faults to show higher discontinuities and displacements in the deeper intervals (IBR), making them more detectable with coherence attributes, than in the upper intervals (top of the Arbuckle and top of the basement), for which curvature and aberrancy would work better.

Moreover, despite focusing on the discontinuities of the IBR that could be correlated with lineaments in the shallowest horizons, it was possible to see other discontinuous patterns with N-S and NE-SW directions in the IBR. This could be as well an indication of intense deformation and fracturing of the basement, of which the fault planes may not be necessarily seen or possibly tracked in the upper horizons.

When considering the features found within folded structures like L4, L6, L7, and L8, it's important not to dismiss the possibility that these might be connected to positive flower structures. The presence of positive flower structures associated with strike-slip faulting would suggest a transpressional regime, aligning with what other researchers have suggested for various regions in Oklahoma. These suggestions point to a transpressional stress environment and the development of larger faults with seismic indications of faulted reflectors near the basement, as well as potentially faulted anticlinal folds in the upper layers (as mentioned by Liao et al., 2017, and Kolawole et al., 2020).

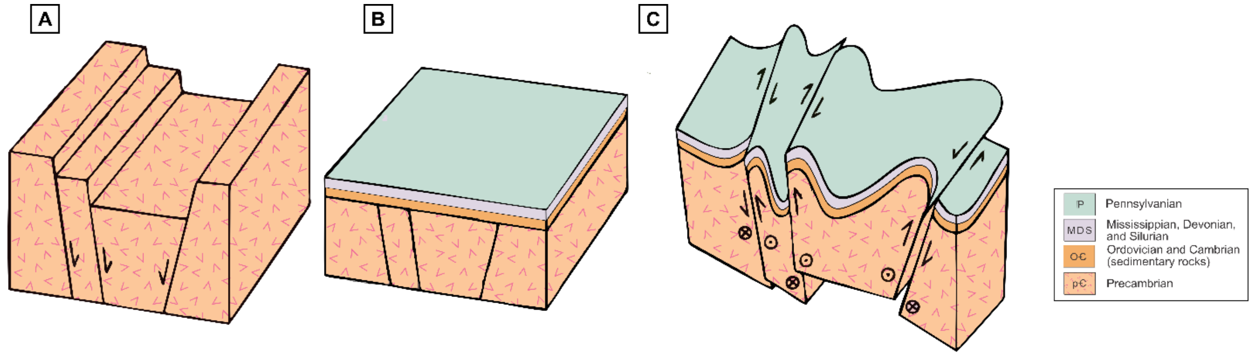

Stage 1. Development of steep basement faults bounding horsts & grabens of the Mid-Continent Rift in the Precambrian (hypothetical).

Stage 2. Erosion of the top basement and deposition of sedimentary rocks in the Early to Mid-Paleozoic.

Stage 3. Late Paleozoic transpressional reactivation of the basement faults create folding and faulting of sedimentary cover rocks.

Figure 2-16. Hypothetical model for the basement faults and connection with upper sedimentary strata in Oklahoma. Modified from Kolawole et al. (2020).

Implications of Seismicity under the Current Oklahoma Stress State

In northcentral Oklahoma, where our study area is located, Qin et al. (2019) found a dominant maximum horizontal stress ranging from 80° – 90° and defined a regime of strike-slip type using focal mechanisms solutions. The authors mapped the reactivated faults in the area using relocated earthquakes catalogs and found strike angles mainly distributed in the ranges of 55°– 75° (NE-SW) and 105° – 125° (NW-SE), with steeply dipping angles larger than 70°, which they indicated are conjugate features relative to a maximum horizontal compression stress orientation of N85°E in the area.

The observed strikes ranging from 25°/205° to 80°/260° and the near 60° degrees difference would indicate a potential conjugate faulting in our area as well. These strike directions are also similar to those observed with earthquake data, which would indicate that some of the mapped potential basement-rooted faults could have strikes favorable for reactivation under the current stress state of Oklahoma if the conditions are met.

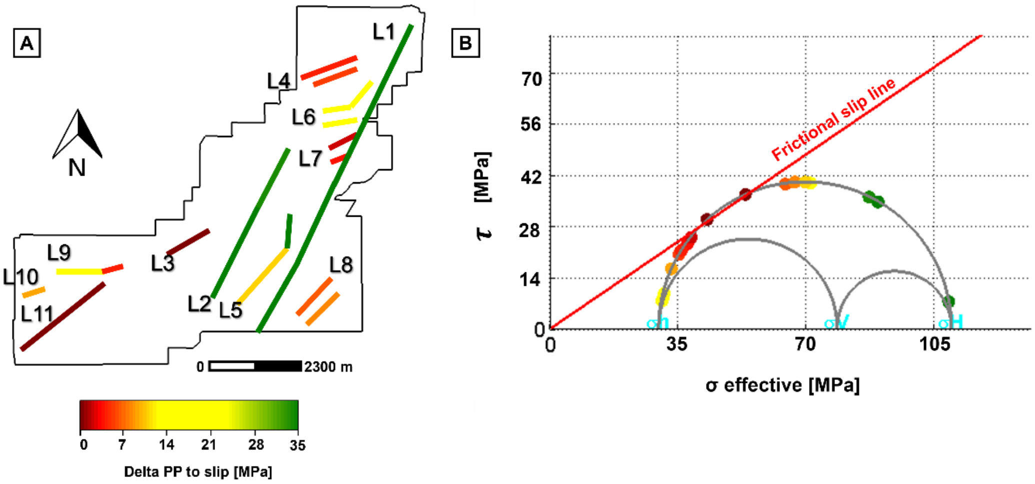

Figure 2-17 Fault slip potential analysis. A) Fault map color code according to the delta pore pressure required to make the fault slip and B) Mohr-Coulomb diagram results.

To check which of the potential basement-rooted faults mapped had strikes more favorable for reactivation, we assessed the fault slip potential (FSP) using the methodology presented by Walsh et al. (2017). This methodology provides a single deterministic calculation of the Mohr-Coulomb pore pressure to slip for each fault using as input the fault geometry, the orientation and magnitudes of the stress field, and the coefficient of friction of the material. More specifically, we plotted 1) the Mohr diagram, taking into account the stress field magnitudes, 2) the stress state of each fault, which are calculated based on the fault strike and dip, and 3) the frictional slip line, which takes into account the coefficient of friction. The pore pressure to slip for each fault is determined as the horizontal distance from the corresponding fault stress state points to the frictional slip line. Since the approach is deterministic, we assume no uncertainty on the input parameters. To have a more probabilistic assessment of FSP, we would need more information regarding the ranges of variability of the input parameters.

Figure 2-17 indicates the FSP results of the lineaments interpreted. We used a SHmax direction of 85°, as in Qin et al. (2019), and a reference depth of 5 km for the rest of the parameters. The specific details of the stress data used can be found in the Appendix, Tables 3 and 4. Observe that the two largest potential basement-rooted faults in the area, L1 and L2, have the strikes least favorable for reactivation, while the potential basement rooted faults that are inferred to bound the folded structures, L4, L6, L7, L8, have strikes that would potentially have reactivation if the delta pore pressure varied between ~10 and ~25 MPa. On the other hand, we can see how structures such as L11 and L3 are the closest to slip under minimum changes in pore pressure. Overall, this correlates with the earthquake data; L11, L10, and the easternmost tip of the potential fault L9, showed seismicity, indicating there has been slip of those faults. These faults showed strikes favorable to slip in the FSP analysis of Figure 2-17.

Finally, the potential basement-rooted faults mapped in our dataset showed near-vertical dip with values larger than 80°. We can infer that these potential faults are near vertical structures that are rooted in the basement and propagated into the overlying sedimentary strata. The exact timing of events is out of the scope of the project, however, the folding of the sedimentary structures far above the Arbuckle would at least indicate a relative post-Ordovician deformation. Additionally, the fact that the observed lineaments extend above the Arbuckle would as well be a crucial observation regarding the structural connectivity and fluid pathways between the interval of wastewater injection, the Arbuckle, and the interval of seismicity, the basement.

CONCLUSIONS

This study's findings align with previous research on Oklahoma's basement faults, which suggests that these faults were pre-existent faults that propagated into the sedimentary section and were recently reactivated through wastewater injection. The detection of higher discontinuities and displacements in the deeper intervals (IBR) reinforces the existent intense basement deformation despite the pre-seismicity belief of an intact basement in northcentral Oklahoma.

The geometry of the mapped potential basement-rooted faults, their similarity with already reactivated faults in the area, and the fault slip analysis under the current stress state of Oklahoma indicate that many of these newly interpreted NE-SW faults have strikes favorable for reactivation if the conditions on pore pressure change are met. Moreover, the positively folded structures seen in the upper horizons could not only be evidence of propagation of basement-rooted faults in the upper sedimentary strata but could also be inferred to be associated with a transpressional regime. However, more details regarding the kinematics of the inferred structures would be needed to complement this matter.

The integration of different geometric attributes through unsupervised ML methods was shown to be a promising approach for identifying previously unseen potential basement-rooted faults in Oklahoma. In this study, we have interpreted eleven potential basement-rooted faults of which three, L9, L10, and L11, could be associated with already proven seismogenic faults, and other three, L1, L2, and L5, show a clear fault expression of a basement-rooted fault cutting an IBR and deforming, folding, and locally showing offsets in the upper BR and AR and overlying sedimentary strata. This approach could be extended to other datasets in the area and aid in the interpretation of basement structures as well as help improve structural maps for Oklahoma.

ACKNOWLEDGMENTS

The authors kindly thank Chesapeake Energy Corporation for providing the seismic dataset, the U.S. Geological Survey (USGS), the Oklahoma Geological Survey (OGS), Enverus, and the FracTracker Alliance for their public databases that were of great support in this project. The authors also thank the sponsors of the Attribute Assisted Seismic Processing and Interpretation (AASPI) consortium for their funding, Schlumberger for the donation of the software Petrel, CGG for the software Hampson Russell, and the Stanford Center for Induced and Triggered Seismicity for the FSP software. Finally, the authors would like to thank David Lubo Robles and Xiaowei Chen for their technical advice during this project.

REFERENCES

Al Dossary, S., and K. J. Marfurt, 2006, 3D volumetric multispectral estimates of reflector curvature and rotation: Geophysics, 71 (5), P41–P51, doi: 10.1190/1.2242449

Bahorich, M. and S. Farmer, 1995, 3-D seismic discontinuity for faults and stratigraphic features: The coherence cube: The leading edge, 14 (10), 1053– 1058, doi: 10.1190/1.1437077

Bhattacharya, S. and S. Verma, 2019, Application of volumetric seismic attributes for complex fault network characterization on the North Slope, Alaska: Journal of Natural Gas Science and Engineering, 65, 56–67, doi: 10.1016/j.jngse.2019.02.002

Bickford, M.E., W.R. Van Schmus, K.E. Karlstrom, P.A. Mueller, and G.D. Kamenov, 2015, Mesoproterozoic-trans-Laurentian magmatism: A synthesis of continent-wide age distributions, new SIMS U–Pb ages, zircon saturation temperatures, and Hf and Nd isotopic compositions: Precambrian Research, 265, 286-312, doi: 10.1016/j.precamres.2014.11.024

Campbell, J. A. and J. L. Weber, 2006, Wells drilled to basement in Oklahoma. Oklahoma Geological Survey Special Publication 2006-1.

Chase, B. F., F. Kolawole, E.A. Atekwana, B.M. Carpenter, M. Turko, M. Abdelsalam, and C. Finn, 2022, The 180-km-long Meers-Willow fault system in the Southern Oklahoma Aulacogen: A potential U.S mid-continent seismic hazard: Geological Society of America Bulletin, doi: 10.1130/B36363.1

Chen, X., N. Nakata, C. Pennignton, J. Haffener, J. C. Chang, X. He, Z. Zhan, S. Ni, and J.I. Walter, 2017, The Pawnee earthquake as a result of the interplay among injection, faults and foreshocks: Scientific Reports, **7**, 4945, 1 – 18, doi: 10.1038/s41598-017-04992-z

Chopra, S., and K. J. Marfurt, 2007, Curvature attribute applications to 3D surface seismic data: The Leading Edge, 26 (4), 404 – 414, doi: 10.1190/1.2723201

Chopra, S., and K. J. Marfurt, 2011, Interesting pursuits in seismic curvature attribute analysis: CSEG Recorder, 36, 40 – 50.

Chopra, S., and K. J. Marfurt, 2015, Is curvature overrated? No, it depends on the geology: First Break, 33, 45 – 55, doi: 10.3997/1365-2397.2014021

Chopra, S., and K. J. Marfurt, 2018, Coherence attribute applications on seismic data in various Guises – Part 2: Interpretation, 6 (3), T531 – T54, doi: 10.1190/INT-2018-0007.1

Chopra, S. and K. J. Marfurt, 2020, Adopting multispectral dip components for coherence and curvature attribute computation: The Leading Edge: 39 (8), 593 – 596, doi: 10.1190/tle39080593.1

Crain, K. and J. Chang, 2018, Elevation map of the top of the crystalline basement in Oklahoma and surrounding states: Oklahoma Geological Survey, Open-File Report 1–2018.

Denison, R.E., 1981, Basement Rocks in Northeastern Oklahoma: Oklahoma Geological Survey, Circular 84.

Drake, R.M., II, and J.R. Hatch, 2021, Geologic Assessment of Undiscovered Oil and Gas Resources in the Cherokee Platform Province Area of Kansas, Oklahoma, and Missouri: U.S. Geological Survey Scientific Investigations Report 2020 – 5110, doi: 10.3133/sir20205110

Elebiju, O.O., S. Matson, G. R. Keller, and K.J. Marfurt, 2011, Integrated geophysical studies of the basement structures, the Mississippi chert, and the Arbuckle Group of Osage County region, Oklahoma: AAPG Bulletin, 95, 371 – 393, doi: 10.1306/08241009154.

Fehmers, G. C., and C. F. W. Höcker, 2003, Fast structural interpretation with structure-oriented filtering: Geophysics, 68 (4), 1286 – 1293, doi: 10.1190/1.1598121

Firkins, M., F. Kolawole, K.J. Marfurt, and B.M. Carpenter, Attribute-assisted characterization of basement faulting and the associated sedimentary sequence deformation in north-central Oklahoma: Interpretation, 8 (4), SP175 – SP189, doi: 10.1190/INT-2020-0053.1

Gao, D., 2013, Integrating 3D seismic curvature and curvature gradient attributes for fracture characterization: Methodologies and interpretational implications: Geophysics, 78 (2), O21 – 031, doi: 10.1190/geo2012-0190.1

Gao, D., and H. Di, 2015, Extreme curvature and extreme flexure analysis for fracture characterization from 3D seismic data: New analytical algorithms and geologic implications: Geophysics, 80 (2), IM11– IM20, doi: 10.1190/GEO2014-0185.1

Guo, H., K. J. Marfurt, and J. Liu, 2009, Principal component spectral analysis: Geophysics, 74 (4), P35 – P43, doi: 10.1190/1.3119264

Ha, T., D. Lubo-Robles, K. Marfurt, and B. Wallet, 2021, An in-depth analysis of logarithmic data transformation and per-class normalization in ML: Application to unsupervised classification of a turbidite system in the Canterbury Basin, New Zealand, and supervised classification of salt in the Eugene Island minibasin, Gulf of Mexico: Interpretation, 9(3), T685 – T710, doi: 10.1190/INT-2021-0008.1

Hames, W.E., Hogan, J.P., and Gilbert, M.C., 1995, Revised Granite-Gabbro Age Relationships, Southern Oklahoma Aulacogen U.S.A, *in* Hogan, J. P. and M.C. Gilbert, 1995, Basement tectonics 12 Central North America and Other Regions, Proceedings of the Twelfth International Conference on Basement Tectonics, held in Norman, Oklahoma, U.S.A., doi: 10.1007/978-94-011-5098-9

Hamilton, M., B.M. Carpenter, C. Johnston, F. Kolawole, S. Evans, and R.D. Elmore, 2021, Fractured, altered, and faulted basement in northeastern Oklahoma: Implications for induced seismicity, Journal of Structural Geology, 147, 2021, doi: 10.1016/j.jsg.2021.104330

Hogan, J.P., and Gilbert, C., 1995, The Southern Oklahoma Aulacogen: A Cambrian analog for Mid-Proterozoic AMCG (Anorthosite-Mangerite-Chamockite-Granite) complexes?, *in* Hogan, J. P. and M.C. Gilbert, 1995, Basement tectonics 12 Central North America and Other Regions, Proceedings of the Twelfth International Conference on Basement Tectonics, held in Norman, Oklahoma, U.S.A., doi: 10.1007/978-94-011-5098-9

Hogan, J. P. and M.C. Gilbert, 1995, Basement tectonics 12 Central North America and Other Regions, Proceedings of the Twelfth International Conference on Basement Tectonics, held in Norman, Oklahoma, U.S.A., doi: 10.1007/978-94-011-5098-9

Hogan, J.P., Gilber, C., Wright, J.E., and Deggeller, M., 1995, Crustal Growth During Continental Rifting: An Example From The Southern Oklahoma Aulacogen, *in* Hogan, J. P. and M.C. Gilbert, 1995, Basement tectonics 12 Central North America and Other Regions, Proceedings of the Twelfth International Conference on Basement Tectonics, held in Norman, Oklahoma, U.S.A., doi: 10.1007/978-94-011-5098-9

Johnson, K., 2008, Geological history of Oklahoma: Oklahoma Geological Survey, Educational Publication, 9.

Kolawole, F., C.S. Johnston, C.B. Morgan, J.C. Chang, K.J. Marfurt, D.A. Lockner, Z. Reches, and B.M. Carpenter, 2019, The susceptibility of Oklahoma's basement to seismic reactivation: Nature Geoscience, 12 (10), 839 – 844, doi: 10.1038/s41561-019-0440-5

Kolawole, F., M. Simpson Turko, and B.M. Carpenter, 2020, Basement-controlled deformation of sedimentary sequences, Anadarko shelf, Oklahoma: Basin Research, 32 (6), 1365 – 1387, doi: 10.1111/bre.12433

Li, F., J. Qi, B. Lyu, and K. J. Marfurt, 2018, Multispectral coherence: Interpretation, 6, T61 – T69, doi : 10.1190/INT-2017-0112.1

Liao, Z., H. Liu, Z. Jiang, K. J. Marfurt, and Z. Reches, 2017, Fault damage zone at subsurface: A case study using 3D seismic attributes and a clay model analog for the Anadarko Basin, Oklahoma: Interpretation, 5, T143 – T150, doi: 10.1190/INT-2016-0033.1

Luo, Y., M. Marhoon, S. Al Dossary, and M. Alfaraj, 2002, Edge-preserving smoothing and applications: The Leading Edge, 21 (2), 136 – 158, doi: 10.1190/1.1452603

Lyu, B., J. Qi, F. Li, Y. Hu, T. Zhao, S. Verma, and K. J. Marfurt, 2020, Multispectral coherence: Which decomposition should we use?: Interpretation, 8 (1), T115 – T129, doi: 10.1190/INT-2019-0124.1

Marfurt, K.J., R.L. Kirlin, S. L. Farmer, M. S. Bahorich, 1998, 3-D seismic attributes using a semblance-based coherency algorithm: Geophysics, 63, 1150 – 1165, doi: 10.1190/1.1444415

Marfurt, K.J., 2006, Robust estimates of 3D reflector dip and azimuth: Geophysics, 71 (4), P29 – P40, doi: 10.1190/1.2213049

Mora, J.P., H. Bedle, and K.J. Marfurt, 2022, Fault enhancement using probabilistic neural networks and Laplacian of a Gaussian filter: A case study in the Great South Basin, New Zealand: Interpretation, 10, SC1-SC15, doi: 10.1190/INT-2021-0127.1

Park, Y., G. C. Beroza, and W. L. Ellsworth, 2022, Basement Fault Activation before Larger Earthquakes in Oklahoma and Kansas: The Seismic Record, 2, 197 – 206, doi: 10.1785/0320220020.

Patel, S., F. Kolawole, J. I. Walter, X. Chen, and K. J. Marfurt, 2021, Seismic illumination of small-throw seismogenic faults, Anadarko Basin, Oklahoma: Interpretation, 9, SE35 – SE5, doi: 10.1190/INT-2020-0135.1

Perico, E. 2021, Application of seismic attributes and machine learning clustering techniques to the characterization of faults in a post-salt reservoir, Jubarte Field (Campos Basin). Master Thesis. University of Oklahoma.

Qi, J., C. Laudon, K.J. Marfurt, 2022, An integrated machine learning-based fault classification workflow: SEG Technical Program Expanded Abstracts: 1865 – 1869, doi: 10.1190/image2022-3750831.1

Qi, J., Lyu, B., Wu, X., and Marfurt, K., 2020, Comparing convolutional neural networking and image processing seismic fault detection methods: SEG Expanded abstracts, 1111 – 1115, doi: 10.1190/segam2020-3428171.1.

Qi, X., and K. J. Marfurt, 2018, Volumetric aberrancy to map subtle faults and flexures: Interpretation, 6, T349 – T365, doi: 10.1190/segam2017-17632807.1

Qin, Y., Chen, X., Walter, J. I., Haffener, J., Trugman, D. T., Carpenter, B. M., et al. (2019). Deciphering the stress state of seismogenic faults in Oklahoma and southern Kansas based on an improved stress map. Journal Geophysical Research: Solid Earth, 124, 12920 –12934, doi: 10.1029/2019JB018377

Ratre, P., 2021, Investigating the regional and local structure of Oklahoma’s crust using induced earthquakes: PhD. Thesis, The University of Oklahoma.

Roy, A., K. J. Marfurt, and M. C. Matos, 2011, Application of 3D clustering analysis for deep water marine Seismic facies classification-an example from deep water Northern Gulf of Mexico: GCSSEPM, 410 – 441, doi: 10.5724/gcs.11.31.0410

Roy A, A. Romero-Peláez, T. Kwiatkowski, K. Marfurt, 2014, Generative topographic mapping for seismic facies estimation of a carbonate wash, Veracruz Basin, southern Mexico: Interpretation, 2(1), SA31 – SA47, doi: 10.1190/INT-2013-0077.1

Skoumal, R., J. O. Kaven, J.I. Walter, 2019, Characterizing seismogenic fault structures in Oklahoma using a relocated template-matched catalog: Seismological Research Letters, 90 (4), 1535 – 1543, doi: 10.1785/0220190045

Tan, J., C.A. Langston, S. Ni, 2021, Shallow shear-wave velocity structure in Oklahoma based on the joint inversion of ambient noise dispersion and teleseismic P-wave receiver functions: Bulletin of the Seismological Society of America, 111(2), 654 – 670.

Taner, M.T., 2001, Seismic attributes: CSEG Recorder, 26 (7), 49 – 56.

Verma, S., S. Chopra, T. Ha, and F. Li, 2022, A review of some amplitude-based seismic geometric attributes and their applications: Interpretation, 10 (1), B1 – B12, doi: 10.1190/INT-2021-0136.1.

Walsh, R., M. D. Zoback, S. P. Lele, D. Pais, M. Weingarten, and T. Tyrrell, 2017, FSP 2.0 A program for probabilistic estimation of fault slip potential resulting from fluid injection, *in* User Guide from the Stanford Center for Induced and Triggered Seismicity, 1– 46.

Wu X., Liang, L., Shi, Y., and Fomel, S., 2019, FaultSeg3D: Using synthetic data sets to train an end-to-end convolutional neural network for 3D seismic fault segmentation. Geophysics, 84 (3), IM 35 – IM 45, doi: 10.1190/geo2018-0646.1.

Wu, X., Shi, Y., Fomel, S., and Liang, L., 2018, Convolutional neural networks for fault interpretation in seismic images. SEG Expanded abstracts, 1946 – 1950, doi: 10.1190/segam2018-2995341.1

Zhao, T., V. Jayaram, A. Roy, and K. J. Marfurt, 2015b, A comparison of classification techniques for seismic facies recognition: Interpretation, 3 (4), SAE29 – SAE58, doi: 10.1190/INT-2015-0044.1

Zhao, T., J. Zhang, F. Li, and K. J. Marfurt, 2016, Characterizing a turbidite system in Canterbury Basin, New Zealand, using seismic attributes and distance-preserving self-organizing maps: Interpretation, 4 (1), SB79 – SB89, doi: 10.1190/INT-2015-0094.1.

APPENDIX

APPENDIX A. 1D Velocity Model

Appendix. Table 1. Shear wave velocity and calculated compressional wave velocity using a Vp/Vs ratio of 1.73. The input P-velocity was averaged for the first 1.5 km.

Depth Range(km)	S-velocity(km/s)	P-velocity [km/s]	Input P-velocity [km/s]
0~0.5	1.215	2.101	3.520
0.5~1	2.170	3.755	3.520
1~1.5	2.718	4.703	3.520
1.5~2	2.910	5.034	5.034
2~2.5	3.178	5.498	5.498
2.5~3	3.323	5.750	5.750
3~3.5	3.416	5.909	5.909
3.5~4	3.384	5.855	5.855
4~4.5	3.456	5.978	5.978
4.5~5	3.526	6.100	6.100
5~5.5	3.507	6.067	6.067
5.5~6	3.529	6.105	6.105
6~6.5	3.559	6.157	6.157
6.5~7	3.586	6.203	6.203
7~7.5	3.629	6.278	6.278
7.5~8	3.652	6.318	6.318
8~8.5	3.637	6.292	6.292
8.5~9	3.614	6.253	6.253
9~9.5	3.634	6.287	6.287
9.5~10	3.663	6.337	6.337

APPENDIX B. Earthquake Lineaments Mapped

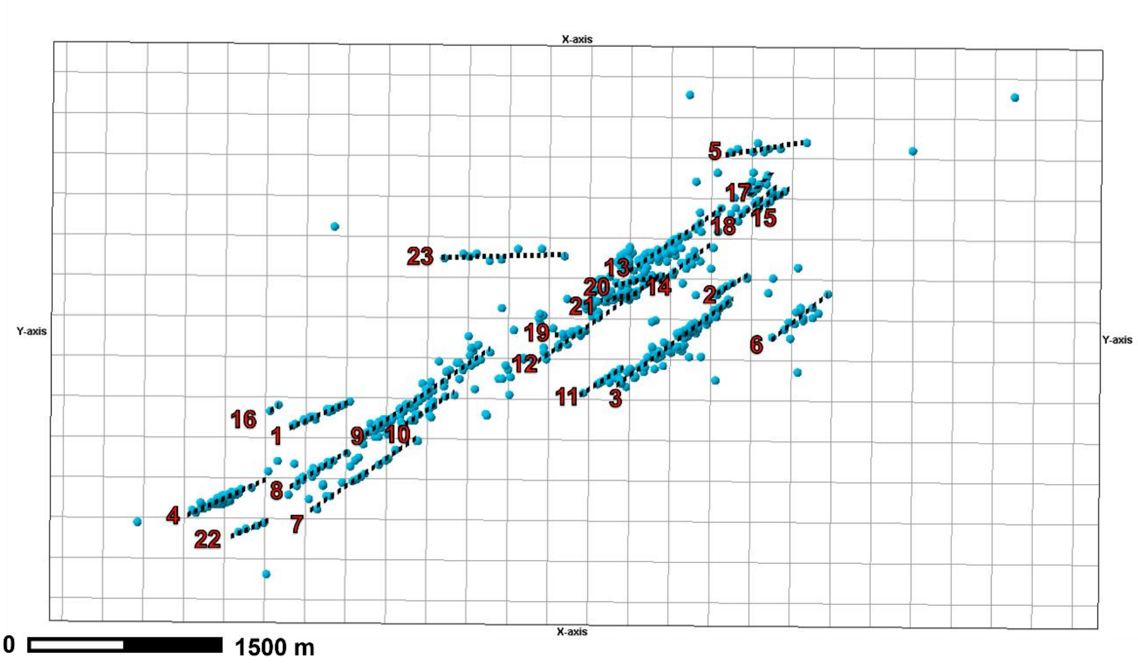

Appendix. Figure 1. Lineaments mapped from visual clustering of earthquake data.

Appendix. Table 2. Estimated strikes of the lineaments mapped using the visual clustering of earthquake data.

Lineament	Strike	Lineament	Strike
1	66	**13**	55
2	59	**14**	53
3	53	**15**	56
4	65	**16**	54
5	80	**17**	44
6	51	**18**	50
7	55	**19**	80
8	58	**20**	78
9	55	**21**	78
10	56	**22**	66
11	57	**23**	88
12	54		

APPENDIX C. Input Parameters for Fault Slip Potential Analysis

Appendix. Table 3. Values used as stress data input for the fault slip potential assessment. Parameters marked with * were taken from Chase et al. (2020)

Parameter	Input value	Comments
Vertical Stress Gradient	1.102 psi/ft	Assuming a value equal to 124.6 MPa calculated as the overburden pressure at 5 km depth. Density of the sedimentary section assumed as 2.71 g/cm3 (limestone) for the first 1 km, and 2.5 g/cm^3 (rhyolite) for the 4 km of basement.
Maximum Horizontal Stress Gradient	1.374 psi/ft	Assuming the estimated mean SHmax magnitude value of 155.4 MPa for Oklahoma *
Minimum Horizontal Stress Gradient	0.677 psi/ft	Assuming the estimated mean SHmin magnitude value of 76.6 MPa for Oklahoma *
Initial Pore Pressure Gradient	0.420 psi/ft	Assuming an estimated mean value of 47.5 MPa at 5 km *
Maximum Horizontal Stress Direction	85°	Mean SHmax for northcentral Oklahoma (Qin et al. 2019)
Coefficient of Friction	0.68	For Oklahoma granite basement faults *
Reference Depth for Calculation	16404.2 ft	Reference 5 km depth for the seismic events

Appendix. Table 4. Fault geometry values used as input data for the fault slip potential assessment.

Fault List	Strike [Degrees]	Dip [Degrees]	Length [km]
L1	205	84	8.839
L2_1	205	86	2.195
L2_2	207	85	1.737
L3	61	90	1.219
L4_1	69	87	1.432
L4_2	250	86	1.189
L5_1	220	86	2.012
L5_2	180	86	0.762
L6_1	81	83	0.701
L6_1_1	39	82	0.792
L6_2	260	82	0.792

L7_1	66	84	0.762
L7_2	248	81	0.610
L8_1	222	89	0.914
L8_2	44	83	1.219
L9_1	89	84	1.158
L9_2	69	86	0.457
L10	73	89	0.640
L11	52	89	2.865